

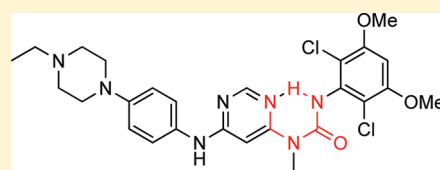
# Discovery of 3-(2,6-Dichloro-3,5-dimethoxy-phenyl)-1-{6-[4-(4-ethyl-piperazin-1-yl)-phenylamino]-pyrimidin-4-yl}-1-methyl-urea (NVP-BGJ398), A Potent and Selective Inhibitor of the Fibroblast Growth Factor Receptor Family of Receptor Tyrosine Kinase

Vito Guagnano,\* Pascal Furet, Carsten Spanka, Vincent Bordas, Mickaël Le Douget, Christelle Stamm, Josef Bruegggen, Michael R. Jensen, Christian Schnell, Herbert Schmid, Markus Wartmann, Joerg Berghausen,† Peter Drueckes, Alfred Zimmerlin, Dirksen Bussiere,§ Jeremy Murray,† and Diana Graus Porta\*

Novartis Institute for BioMedical Research, CH-4002 Basel, Switzerland

**S** Supporting Information

**ABSTRACT:** A novel series of *N*-aryl-*N'*-pyrimidin-4-yl ureas has been optimized to afford potent and selective inhibitors of the fibroblast growth factor receptor tyrosine kinases 1, 2, and 3 by rationally designing the substitution pattern of the aryl ring. On the basis of its *in vitro* profile, compound **1h** (NVP-BGJ398) was selected for *in vivo* evaluation and showed significant antitumor activity in RT112 bladder cancer xenografts models overexpressing wild-type FGFR3. These results support the potential therapeutic use of **1h** as a new anticancer agent.



**1h (NVP-BGJ398)**

## INTRODUCTION

During the past 15 years, the pharmaceutical industry has shown an ever-growing interest in the field of tyrosine kinases. Among this class of enzymes, the fibroblast growth factor receptor (FGFR) family represents an attractive therapeutic target in oncology that is gaining increasing attention. The fibroblast growth factor receptor (FGFR) family of receptor tyrosine kinases (RTKs) comprises four members (FGFR1, FGFR2, FGFR3, and FGFR4) that share significant sequence homology. Each receptor consists of an extracellular ligand-binding domain containing three immunoglobulin-like repeats, a single transmembrane domain, and a cytosolic region with a split tyrosine kinase domain and tyrosine autophosphorylation sites. This family of RTKs serves as high affinity receptors for the fibroblast growth factors (FGFs) that control cell proliferation, migration, apoptosis, and differentiation and are involved in both developmental and adult tissue homeostasis.<sup>1</sup>

A variety of genetic alterations, including deregulated expression and/or abnormal activation of FGFs and FGFR family members, has been found in diverse tumor types.<sup>2</sup> Translocation and fusion of FGFR1 to other genes resulting in constitutive activation of its kinase by oligomerization is responsible for 8p11 myeloproliferative disorder (MPD).<sup>3–8</sup> PKC412,<sup>9</sup> a compound which inhibits the growth of ZNF198–FGFR1-transformed BaF3 cells with an IC<sub>50</sub> of 200 nM, proved efficacious when administered to one patient with MPD.<sup>10</sup> Similar translocations and fusions for FGFR3 are associated with peripheral T-cell lymphoma.<sup>11</sup> In multiple myeloma, recurrent chromosomal translocations of 14q32 into the immunoglobulin heavy chain switch region result in deregulated overexpression of

FGFR3.<sup>12–14</sup> Further, somatic activating mutations in FGFR3 in solid tumors, being particularly high in bladder carcinomas,<sup>15–17</sup> and activating point mutations of FGFR2 in gastric cancer<sup>18–20</sup> and in endometrial carcinomas<sup>21</sup> have been described. Recently, frequent and focal FGFR1 amplification has been identified in squamous cell lung cancer and found to be associated with tumor growth and survival.<sup>22</sup> Gene amplification and protein overexpression have been reported for FGFR1, FGFR2, and FGFR4 in breast cancer.<sup>23–28</sup> Specifically for FGFR1, the amplification of the locus was significantly more prevalent in tumors that lacked HER2 and proved to be an independent prognostic factor for poor overall survival in estrogen receptor (ER) positive breast cancer patients.<sup>29</sup> In breast tumors, the 11q13 amplicon containing three different FGFs (FGF3, FGF4, and FGF19) has been found amplified.<sup>30–33</sup> Interestingly, FGF3 and FGF4 are two of the most commonly activated oncogenes upon mouse mammary tumor virus (MMTV) insertion in the mouse genome, leading to mammary tumors. Other tumor types in which this amplicon is altered include ovarian tumors,<sup>34,35</sup> oral squamous cell carcinomas,<sup>36</sup> and hepatocellular carcinomas.<sup>37,38</sup>

While there are a number of low molecular weight compounds in clinical development (such as BIBF-1120,<sup>39</sup> TKI258,<sup>40</sup> BMS-582664,<sup>41</sup> AZD-2171,<sup>42,43</sup> AB-1010,<sup>44</sup> TSU-68,<sup>45</sup> AP-24534,<sup>46</sup> and E-7080,<sup>47,48</sup> shown in Figure 1) that are reported to target FGFR, they have multitarget specificity with respect to other kinases.

The quest for highly selective small molecule inhibitors of specific kinases is still a significant challenge for medicinal

**Received:** May 17, 2011

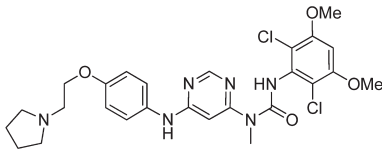
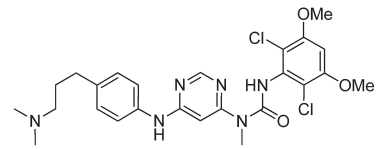
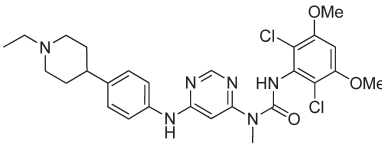
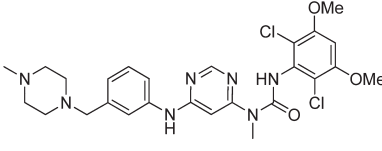
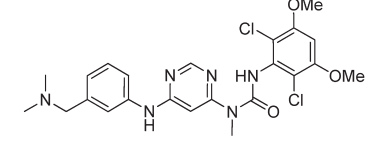
**Published:** September 21, 2011



Table 1. Structures and FGFR3 Biochemical and Cellular Potencies of *N*-Aryl-*N'*-pyrimidin-4-yl Ureas

Compd	Structure	IC <sub>50</sub> (nM) <sup>b</sup>	
		FGFR3-K650E kinase inhibition <sup>a</sup>	BaF3-TEL-FGFR3 cells proliferation inhibition
1a		505	1512
1b		125	635
1c		66	832
1d		115	750
1e		840	2223
1f		51	126
1g		54	118
1h		5	2
1i		9	2

Table 1. Continued

Compd	Structure	IC <sub>50</sub> (nM) <sup>b</sup>	
		FGFR3-K650E kinase inhibition <sup>a</sup>	BaF3-TEL-FGFR3 cells proliferation inhibition
1j		16	28
1k		11	27
1l		7	14
1m		20	14
1n		19	11

<sup>a</sup> Radiometric kinase assay. <sup>b</sup> Single measurement.

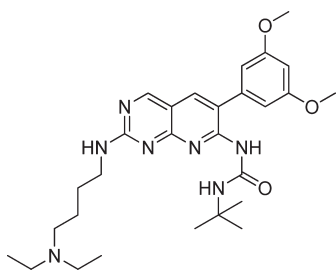


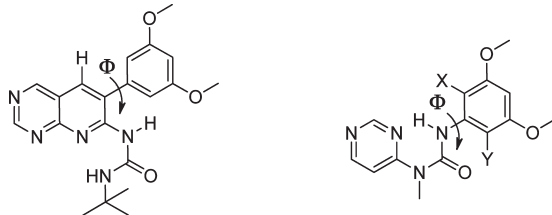
Figure 3. Chemical structure of compound 3 (PD173074).

using a FGFR3-dependent BaF3 cell line, and a homology model of the FGFR3 kinase domain. Taking into account the high level of sequence homology among the four members of the FGFR family,<sup>51</sup> FGFR3 was selected for screening purposes owing to the interesting epidemiological data available at the beginning of this program which demonstrated the critical role of this receptor in the pathogenesis of bladder cancer.<sup>15–17</sup> Importantly, we considered the published information concerning known inhibitors of FGFRs and focused on compound 3<sup>52</sup> (PD173074,

Figure 3), an inhibitor displaying selectivity for these receptors that had been crystallized bound to the ATP binding site of the FGFR1 tyrosine kinase domain.<sup>53</sup>

This compound, which belongs to the pyrido[2,3-*d*]pyrimidine class, exhibits nanomolar and submicromolar inhibitory activity at the cellular level against FGFR1 and VEGFR2, respectively.<sup>53</sup> Its high affinity and selectivity for FGFR1 stem from the presence at the C(3) and C(5) positions of the phenyl ring of two methoxy groups that fill optimally a complementary hydrophobic pocket in the cocrystal structure. As an entry to our lead optimization process, we took advantage of this finding and introduced the 3,5-dimethoxy-phenyl pharmacophore in the pyrimidinyl urea scaffold by preparing compound 1a (Table 1).

We expected that 1a would exhibit lower potency than 3 due to the significantly higher deconjugation energy barrier that the dimethoxy-phenyl moiety of the former compound has to overcome to adopt an almost perpendicular orientation required for binding to the kinase ATP pocket as revealed by the 3-FGFR1 cocrystal structure. Ab initio calculations (Table 2) indicate that this deconjugation has an energy cost of 1.5 kcal/mol in 1a, taking the relaxed conformation of the compound in water as

**Table 2.** Difference in Energy between the Constrained and Unconstrained Minimized Structure of **3**, **1a**, **1b**, and **1h**


	compd			
	<b>3</b>	<b>1a</b>	<b>1b</b>	<b>1h</b>
$\Phi_{\text{low}}^a$	127	180	180	109
$\Delta E^b$	0.5	1.5	1.1	0.1

<sup>a</sup> Torsion angle ( $\Phi$ ) value in degrees in the unconstrained minimized structure. <sup>b</sup> Difference in energy ( $\Delta E$ ) in kcal/mol between the constrained (kinase bound) and unconstrained minimized structure.

**Table 3.** Profile of Compounds **1h–n** in a Panel of Human Cytochrome P450 Isozymes

compd	IC <sub>50</sub> ( $\mu$ M) for CYP450/substrate <sup>a</sup>					
	3A4/ BFC	3A4/ DBF	2C9/ MFC	2C19/ CEC	2D6/ AMMC	1A2/ CEC
<b>1h</b>	>10	>10	>10	>10	>10	>10
<b>1i</b>	1.1	>10	1.7	0.9	>10	>10
<b>1j</b>	>10	2.5	>10	>10	>10	>10
<b>1k</b>	1.0	>10	>10	3.6	>10	>10
<b>1l</b>	1.2	6.0	4.0	1.1	>10	>10
<b>1m</b>	0.5	>10	>10	0.3	>10	7.0
<b>1n</b>	<0.1	2.5	>10	1.4	>10	>10

<sup>a</sup> 7-Benzyloxy-4-(trifluoromethyl)-coumarin (BFC), dibenzylfluorescein (DBF), 7-methoxy-4-trifluoromethylcoumarin (MFC), 3-cyano-7-ethoxycoumarin (CEC), 3-[2-(*N,N*-diethyl-*N*-methylamino)ethyl]-7-methoxy-4-methylcoumarin (AMMC).

reference. In contrast, this cost amounts to only 0.5 kcal/mol for **3** because higher intramolecular steric hindrance in this compound causes its reference minimum energy conformation to be closer to the perpendicular, kinase bound conformation.

Indeed, **1a** showed only moderate submicromolar inhibitory activity (IC<sub>50</sub> 505 nM) against the FGFR3 kinase in the biochemical assay and inhibited the proliferation of the BaF3-Tel-FGFR3 cell line with an IC<sub>50</sub> value of 1.5  $\mu$ M. To lower the deconjugation energy penalty in **1a**, we envisaged the introduction of chlorine atoms in the ortho positions of the dimethoxyphenyl ring. Modeling based on the 3-FGFR1 cocystal structure suggested that, in addition to stabilizing the perpendicular conformation, the chlorine atoms would form favorable hydrophobic contacts with the kinase ATP pocket. This was supported by the significant FGFR1 inhibitory activity (570 nM) displayed by our initial *ortho*-dichloro-prototype compound **2**. On the basis of these considerations, compound **1b** was synthesized which showed improved biochemical and cellular potency (4- and 2.5-fold, respectively), in agreement with the reduction in the calculated deconjugation energy (Table 2). Exchange of the methyl on the urea nitrogen in **1b** by either a hydrogen atom

**Table 4.** Selectivity of **1h** in a Panel of Kinases<sup>a</sup>

kinase	IC <sub>50</sub> ( $\mu$ M)	kinase	IC <sub>50</sub> ( $\mu$ M)
FGFR3	0.0010	ABL	2.3
FGFR3-K650E	0.0049	FYN	1.9
FGFR1	0.0009	KIT	0.75
FGFR2	0.0014	LCK	2.5
FGFR4	0.060	LYN	0.30
VEGFR2	0.18	YES	1.1

<sup>a</sup> All assays were performed with purified recombinant enzymes under optimized conditions using peptidic substrates and a microfluidic mobility shift readout (Caliper lifesciences, Mountain View, CA, USA). The concentrations for ATP were adjusted to the respective  $K_m$  values of the kinase.

**Table 5.** Selectivity of **1h** in a Panel of BaF3 Cells

BaF3 cells	IC <sub>50</sub> (nM)	BaF3 cells	IC <sub>50</sub> (nM)
FGFR3	2.0	VEGFR2-Q <sup>a</sup>	938
FGFR3-Q <sup>a</sup>	0.7	VEGFR1-Q <sup>a</sup>	1510
FGFR3-K650E	52.2	VEGFR3-Q <sup>a</sup>	2072
FGFR1	2.9	BCR-ABL	2192
FGFR2-Q <sup>a</sup>	2.0	KIT-Q <sup>a</sup>	2501
VEGFR2	1449	LYN	3019

<sup>a</sup> Q indicates presence of juxtamembrane domain in the TEL-kinase construct.

(compound **1c**) or an ethyl group (compound **1d**) had a neutral effect on potency. Consistent with the binding hypothesis, removal of the methoxy group at the C(3) position of the urea aniline to give compound **1e** resulted in a decrease of potency. Addition of the second ortho chlorine atom afforded derivatives (**1f–g**) showing double-digit nanomolar activity in the biochemical assay while for the first time approaching the 100 nM level in the proliferation assay. Finally, the most potent compounds (**1h–n**) were obtained when we introduced the optimal 2,6-dichloro-3,5-dimethoxy-phenyl moiety, which is associated to the lowest deconjugation energy and modified the pyrimidinyl aniline to modulate the pharmacological profile.

**Evaluation of Compounds 1h–n in a Cytochrome P450 Panel.** Inhibition of cytochrome P450 (CYP450) drug metabolizing enzymes may alter the metabolism of coadministered compounds, leading to a change in drug exposure and possible toxicity. Thus, the potential for drug–drug interactions of compounds **1h–n** was assessed by monitoring their impact on the metabolic activity of a panel of five major human CYP450 isoforms (3A4, 2C9, 2C19, 2D6, and 1A2) in the presence of a known substrate for each of the isoforms. CYP3A4 inhibition was determined in two assays using two distinct substrates to account for the existence of two substrate binding sites. The results of these six assays, one for each specific isoform/substrate combination, are reported in Table 3.

Whereas compounds **1i–n** inhibited between one and three of the CYP isozymes at single-digit micromolar or submicromolar concentrations, compound **1h** did not show inhibitory activity against any of the isoforms up to the 10  $\mu$ M concentration and was selected for further profiling.

**In Vitro Activity and Selectivity Profile of Compound 1h.** The selectivity of **1h** was first evaluated by testing it against our

in-house panel of 76 protein kinases. Compound **1h** inhibited FGFR1, FGFR2, and FGFR3 with  $IC_{50} = 1$  nM, FGFR3-K650E with  $IC_{50} = 4.9$  nM, and FGFR4 with  $IC_{50} = 60$  nM.  $IC_{50}$  values for all other kinases were greater than  $10 \mu M$  (see Supporting Information) or in the  $\mu M$  range (FYN, LCK, YES, and ABL) except for VEGFR2, KIT, and LYN, which were inhibited at submicromolar concentrations of the compound (Table 4).

At the cellular level, the selectivity of **1h** was determined by measuring its ability to inhibit the proliferation of a panel of 31 BaF3 cell lines. The data summarized in Table 5 show that **1h** inhibited the proliferation of the FGFR1-, FGFR2-, and FGFR3-dependent BaF3 cells with  $IC_{50}$  values which were in the low nanomolar range and comparable to those observed for the inhibition of the receptors kinase activity in the enzymatic assay. For the remaining cells, all  $IC_{50}$  values were greater than  $1.5 \mu M$  (see Supporting Information) except for VEGFR2 ( $IC_{50}$  1449 and 938 nM), for which there was at least a 400-fold selectivity versus FGFR1, FGFR2, and FGFR3.

Because activation of FGFRs results in autophosphorylation on specific tyrosine residues, the ability of **1h** to interfere with FGFR kinase activity at the cellular level was determined by monitoring changes in the phosphotyrosine content of the receptor by means of a capture ELISA assay. Four cell capture ELISA assays that detect pFGFR1, pFGFR2, pFGFR3, and pFGFR4, respectively, were developed using HEK293 cells transfected with expression vectors encoding for the indicated FGFRs. The data summarized in Table 6 show that **1h** inhibited FGFR1, FGFR2, and FGFR3 with a 5 nM  $IC_{50}$  and to a lesser extent FGFR4, in agreement with the trend observed in the biochemical assay (Table 4).

With the aim of developing a disease model to assess the efficacy of **1h**, we tested the compound against a panel of eight human bladder cancer cell lines. In accordance to the observed selectivity profile, **1h** suppressed proliferation of the cancer cells with wild-type (WT) FGFR3 overexpression but not those lacking this receptor (Table 7). Owing to their ability to grow in vivo, the RT112 cells were used to establish disease models in rodents.

**Pharmacokinetics of Compound 1h in Rodents.** Compound **1h** was administered to athymic nude mice implanted subcutaneously with RT112/luc1 tumors: either as a 5 mg/kg intravenous bolus in NMP/PEG200 (1:9, v/v) or orally by gavage as a suspension in PEG300/DSW (2:1, v/v) at a 20 mg/kg dose. The relevant pharmacokinetic (PK) parameters reported in Table 8 indicate that the oral bioavailability of **1h** in

**Table 6.** Cellular Activity of **1h** in Cell Capture ELISA Assay for pFGFR1-4

	receptor				
	FGFR1-WT	FGFR2-WT	FGFR3-K650E	FGFR3-S249C	FGFR4-WT
$IC_{50}$ (nM)	4.6	4.9	5.0	5	168

**Table 7.** Cellular Activity of **1h** in a Panel of Bladder Cancer Cells

	cell line							
	RT112 <sup>a</sup>	RT4 <sup>a</sup>	SW780 <sup>a</sup>	JMSU1 <sup>a</sup>	HT1197	VMCUB1	UMUC3	J82
$IC_{50}$ (nM)	5	30	32	15	1157	>3000	>3000	>3000

<sup>a</sup>Bladder cancer cell lines overexpressing WT FGFR3.

this study was 32%. After intravenous dosing, the compound showed a rapid distribution from the vascular compartment into the peripheral tissues, translating into a high volume of distribution (26 L/kg). The plasma clearance was high at 3.3 L/h/kg (61% of liver blood flow). The ratio of tumor to plasma after oral dosing based on AUC was determined to be 10.

Compound **1h** was administered intravenously to the femoral vein of female Wistar rats as a 5 mg/kg intravenous bolus in NMP/PEG200 (1:9, v/v). The monophosphate salt of **1h** was dosed as an oral solution in acetic acid–acetate buffer pH 4.6/PEG300 (1:1, v/v) at 10 mg/kg. As shown in Table 9, the estimated mean systemic plasma clearance of **1h** was high (3.6 L/h/kg) as compared to the hepatic blood flow (3.3 L/h/kg), while the estimated volume of distribution at steady state ( $V_{ss}$ , 9.6 L/kg) was very high compared to the total body water volume in rats (0.66 L/kg). The apparent terminal elimination half-life in plasma was around 5 h after both intravenous and oral administration. The oral bioavailability of **1h** in this study was 51%.

**Table 8.** Pharmacokinetic Properties of **1h** in RT112 Tumor-Bearing Mice

parameter	unit	iv dose (5 mg/kg)		po dose (20 mg/kg)	
		plasma	tumor	plasma	tumor
$C_{max}$	$\mu M$ or nmol/g <sup>a</sup>	0.86	1.68	0.42	1.63
$t_{max}$	h		2	1	8
$t_{1/2}$	h	9.3	6.7	4.3	13
AUC <sup>b</sup>	$\mu M \cdot h$ or h·nmol/g <sup>c</sup>	0.6	4.8	0.18	1.85
CL	L/h/kg	3.3			
$V_{ss}$	L/kg	26			
$F_{po}$ <sup>d</sup>	%			32	

<sup>a</sup>Plasma in  $\mu M$ , tissues in nmol/g. <sup>b</sup>Dose normalized to 1 mg/kg. <sup>c</sup>Plasma in  $\mu M \cdot h$ , tissues in h·nmol/g. <sup>d</sup>Bioavailability ( $F_{po}$ ) is calculated as dose-normalized  $AUC_{po} / AUC_{iv}$  extrapolated to infinity.

**Table 9.** Pharmacokinetic Properties of **1h** in Wistar Rats

parameter	unit	iv dose (5 mg/kg)	po dose (10 mg/kg)
$C_{max}$	$\mu M$ or nmol/g <sup>a</sup>	0.97 <sup>b</sup>	0.26
$t_{max}$	h		4
$t_{1/2}$	h	4.5	4.8
AUC <sup>c</sup>	$\mu M \cdot h$	0.49	0.25
CL	L/h/kg	3.6	
$V_{ss}$	L/kg	9.6	
$F_{po}$ <sup>d</sup>	%		51

<sup>a</sup>Plasma in  $\mu M$ , tissues in nmol/g. <sup>b</sup>Determined 5 min postadministration. <sup>c</sup>Dose normalized to 1 mg/kg. <sup>d</sup>Bioavailability ( $F_{po}$ ) is calculated as dose-normalized  $AUC_{po} / AUC_{iv}$  extrapolated to infinity.

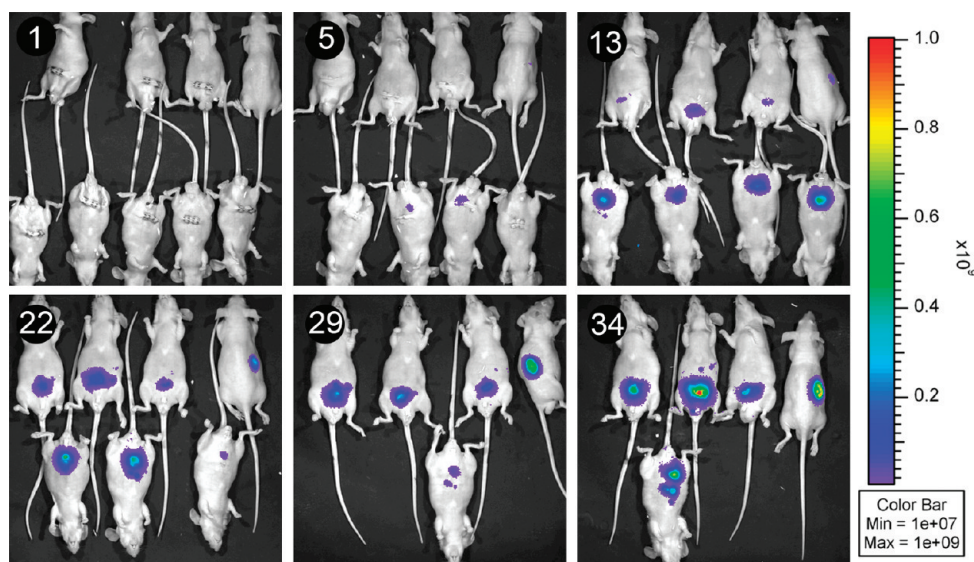


**Figure 4.** Growth kinetics of orthotopically growing RT112/luc1 bladder cancer cells. Tumor burden was monitored by measuring light emission after intravenous injection of D-luciferin. Representative Xenogen IVIS images from 1, 5, 13, 22, 29, and 34 days after inoculation. One animal (top right in each frame) was inoculated subcutaneously for comparison. The pseudocolor gradient of each image has been adjusted to the same scale (right).

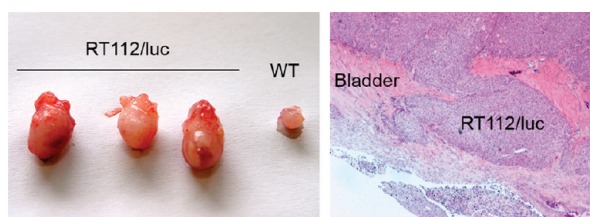


**Figure 5.** Orthotopically growing RT112/luc1 bladder tumors dissected 34 days after inoculation. Left: Three tumor-filled bladders dissected from RT112/luc1 bladder tumor carrying mice. A noninoculated normal bladder (WT) is shown for comparison. Right: Histology of a representative tumor invading through the bladder wall.

**In Vivo Antitumor Activity of Compound 1h.** The anti-tumor activity of **1h** was evaluated in an orthotopic xenograft bladder cancer model based on the human bladder cancer cell line RT112 which overexpresses FGFR3. To establish this model, the parental RT112 cell line was stably infected with a retrovirus that constitutively expresses luciferase (pLNCX2/luc1) to generate RT112/luc1 cells which were suspended in 50% Matrigel and injected into the bladder lumen of female HsdNpa: Athymic Nude-nu mice (Figure 4).

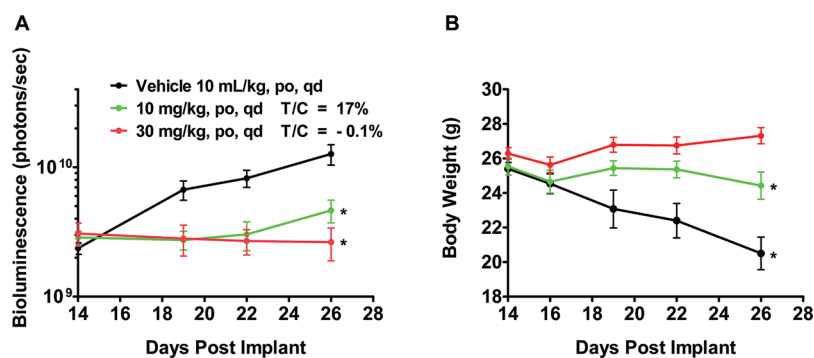
At 34 days after inoculation, the bladders of the tumor bearing animals were increased in size due to the tumor mass compared with a normal bladder. Histological analysis demonstrated that the tumors invade through the bladder wall during the late stages of the study (Figure 5).

When tested in this orthotopic xenograft bladder cancer model, **1h** induced tumor growth inhibition and stasis after oral administration for 12 consecutive days at the doses of 10 and 30 mg/kg, respectively (Figure 6). The experiment was terminated prematurely at treatment day 12 due to a 15% body weight loss observed in the vehicle treated animals as a consequence of the disease progression. Interestingly, the animals that received **1h** exhibited either no body weight loss (10 mg/kg) or 10% body weight gain (30 mg/kg), a further indication of efficacy.

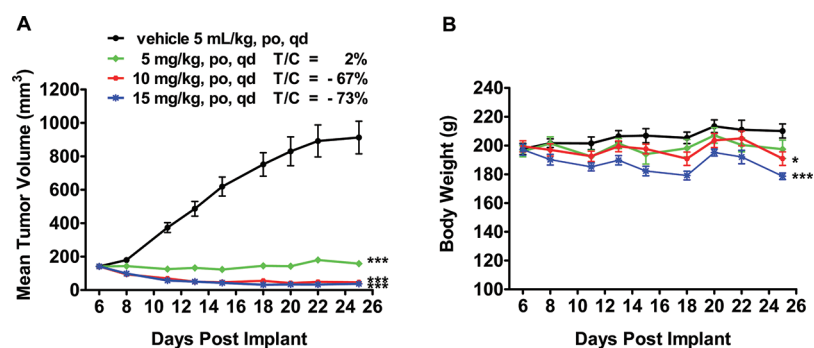
A subcutaneous tumor model using the RT112 human bladder cancer xenograft in rats was established with the aim to determine the correlation between efficacy and tolerability of **1h** in this species. The monophosphate salt of **1h** was orally administered to juvenile, immunocompromised, female Rowett rats ( $n = 8$ ) for 20 consecutive days (20 administrations) at the doses of 5, 10, and 15 mg/kg/qd (free base equivalents). Figure 7 shows the mean tumor growth and mean body weight changes in the course of treatment. Nearly complete tumor stasis was achieved at the lowest dose while no overt toxicity (morbidity or body weight loss) was observed (Figure 7). The doses of 10 and 15 mg/kg provided tumor regression (66% and 73%, respectively) which was accompanied by a dose-dependent decrease of body weight (4% and 9%, respectively).

The relationship between antitumor efficacy and inhibition of the molecular target in vivo was assessed in an independent study. Thus, RT112 tumor-bearing, female Rowett rats ( $n = 4$ ) received a single oral administration of the monophosphate salt of **1h** at the doses of 4.25 and 8.51 mg/kg (free base equivalents) (Figure 8). Tumors were collected at various time points post-therapy for compound concentration determination and pharmacodynamic (PD) analysis. Because FGFRs mediate several cellular responses via phosphorylation of the membrane-anchored docking protein FRS2 which links the activated RTK to intracellular pathways (e.g., Ras-MAPK pathway),<sup>54</sup> pFRS2 and the downstream pMAPK were used as PD markers. Compound **1h** significantly decreased the levels of pFRS2 and pMAPK in a dose-dependent manner. Whereas only partial inhibition of the two markers was observed at the lower dose, their phosphorylation was almost completely abolished up to 16 h in the group treated with the 8.51 mg/kg dose. The inhibitory effect diminished in a time-dependent manner and was completely relieved 24 h postdosing, correlating with compound elimination from the tumor tissue.

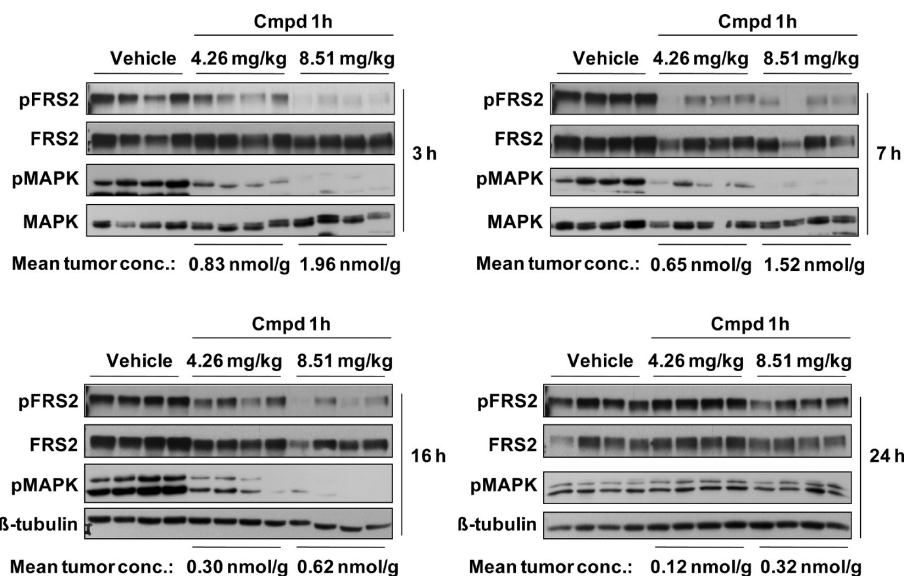
**In Vivo Antiangiogenic Activity of Compound 1h.** The ability of **1h** to inhibit angiogenesis induced by either bFGF or VEGF was tested in vivo in an agar chamber model. Compound **1h** was administered orally in doses of 10, 30, and 50 mg/kg daily for 4 consecutive days to female FVB mice implanted subcutaneously with either bFGF or VEGF containing chambers.



**Figure 6.** Tumors were established in female HsdNpa: Athymic Nude-nu mice by orthotopic inoculation of  $5 \times 10^5$  cells per animal. Daily treatment with compound **1h** administered orally as a suspension in PEG300/DSW (2:1, v/v) at 0, 10, and 30 mg/kg was initiated 14 days after inoculation. (A) Light emission from tumor bearing animals during 12 days treatment as a measure of tumor burden. (B) Body weight measurements during the treatment. Data are presented as means  $\pm$  SEM \* $p < 0.05$ ; ANOVA post hoc Dunnett's versus vehicle treated.



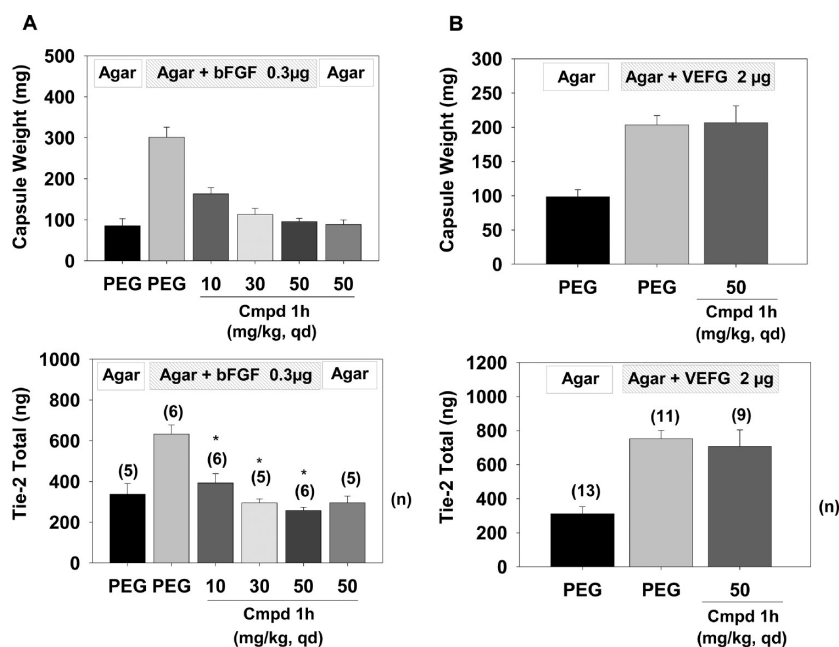
**Figure 7.** (A) Antitumor activity of compound **1h** against RT112 human bladder cancer xenografts implanted subcutaneously in immunocompromised, female Rowett rats. (B) Body weight measurements during the treatment. Data are presented as means  $\pm$  SEM \* $p < 0.05$ , \*\*\* $p < 0.001$ ; ANOVA post hoc Dunnett's versus vehicle treated.



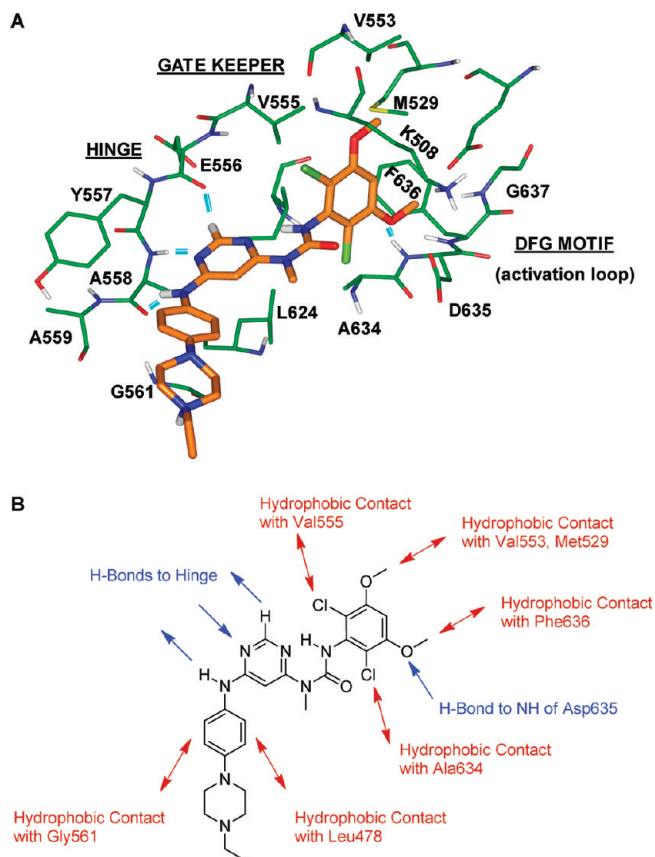
**Figure 8.** RT112 xenograft tumors were dissected at the indicated time points postdosing ( $n = 4$ ), lysed, and analyzed by Western blot for concentration of **1h**, FRS2 Tyr-phosphorylation (pFRS2), and MAPK activation (pMAPK). Protein loading was monitored by analyzing the lysates for total FRS2 protein, total MAPK protein, or  $\beta$ -tubulin.

Upon removal of the chambers 24 h after the last dose, the angiogenic response was quantified by measuring the weight and the Tie-2 (a receptor tyrosine kinase specifically expressed on

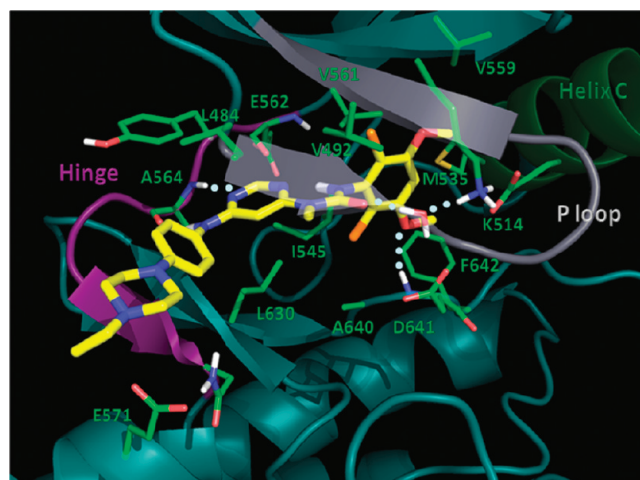
endothelial cells) levels of the vascularized tissue grown around the chamber (capsule). As shown in Figure 9, compound **1h** inhibited significantly bFGF-stimulated angiogenesis in a



**Figure 9.** Effect of 1h treatment on the capsule weight and Tie-2 levels in bFGF (A) or VEGF (B) containing porous chambers implanted subcutaneously in the flank of FVB mice. Animals were treated orally either with 1h at 10, 30, and 50 mg/kg or vehicle (NMP/PEG300 10%, 5 mL/kg) starting 4–6 h before implantation of the chambers and daily for 3 additional days. Values are mean  $\pm$  SEM \* $p$  < 0.05, statistical significance of inhibition.



**Figure 10.** (A) Binding model of 1h to the FGFR3 kinase domain homology model showing interacting residues. Hydrogen bonds are indicated by turquoise dashes. (B) Summary of the interactions of 1h within the ATP binding site of FGFR3.

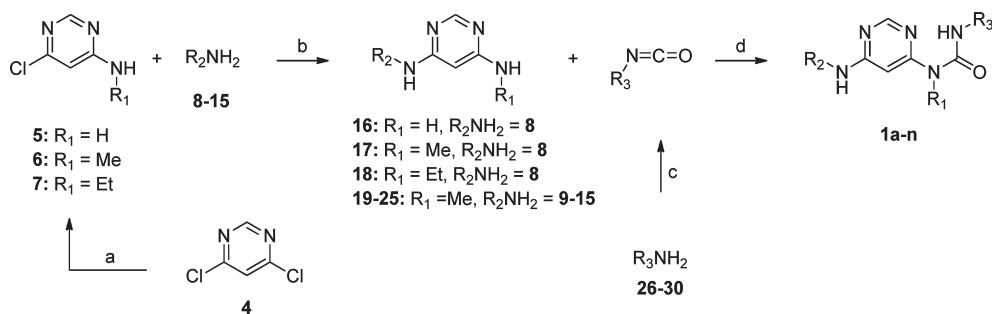


**Figure 11.** X-ray structure of the 1h–FGFR1 complex (RCSB ID: rcsb067881, PDB ID: 3TT0). Hydrogen bonds are indicated by pale cyan circles.

dose-dependent manner. However, it did not impair VEGF-induced blood vessel formation. This result demonstrates the selectivity of 1h for FGFR versus VEGFR.

**Docking of 1h to FGFR3 Kinase Domain Model and X-ray Structure of the FGFR1–Compound 1h Complex.** The proposed binding mode of 1h in the FGFR3 catalytic site and a summary of the interactions of the inhibitor with the enzyme are shown in Figure 10.

According to this model, the 4-(4-ethyl-piperazin-1-yl)-phenylamine NH and the adjacent pyrimidine nitrogen of 1h are involved in critical H-bonds with the carbonyl and the amino group of alanine 558 (an amino acid residue located in the hinge

Scheme 1. General Synthesis of *N*-Aryl-*N'*-pyrimidin-4-yl Ureas<sup>a</sup>

<sup>a</sup> Reagents and conditions: (a) R<sub>1</sub>NH<sub>2</sub>, 25% NH<sub>3</sub> in H<sub>2</sub>O, 33% MeNH<sub>2</sub> in EtOH or 70% EtNH<sub>2</sub> in H<sub>2</sub>O, *i*-PrOH, RT; (b) R<sub>2</sub>NH<sub>2</sub> (8–15), CH<sub>3</sub>COOH/H<sub>2</sub>O, 100 °C or 4 N HCl in dioxane, 150 °C; (c) 20% COCl<sub>2</sub> in toluene, dioxane, reflux; (d) toluene, 70 °C or reflux.

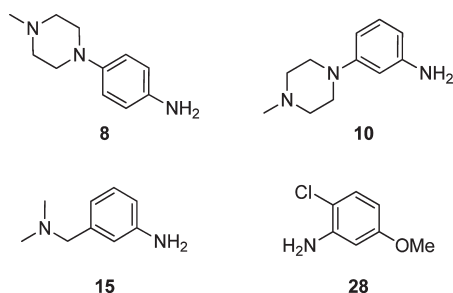


Figure 12. Structures of anilines 8, 10, 15, and 28.

region of the ATP-binding pocket), respectively. An additional H-bond occurs between the backbone carbonyl group of glutamic acid 556 (hinge region) and the pyrimidine C(2)-H, which behaves as a H-bond donor by virtue of the polarization induced by the two adjacent nitrogen atoms. It is noteworthy that the urea carbonyl group might also be engaged in a water-mediated H-bond (not shown) with the side chain amino group of lysine 508, whereas the aryl ring of the 4-(4-ethylpiperazin-1-yl)phenylamine is in contact with the hydrophobic side chains of two amino acid residues glycine 561 and leucine 478 (the latter not represented for clarity) in a sandwich-like manner.

The optimized substitution pattern of the urea aniline is responsible for productive interactions such as the H-bond between the methoxy oxygen and the NH of aspartate 635 in addition to further hydrophobic contacts. The optimal fitting of the tetra-substituted phenyl ring in the complementary hydrophobic cavity results from the perpendicular orientation of this ring with respect to the plane of the pseudobicyclic system. Such a rigid orthogonal arrangement is enforced by the two chlorine atoms which prevent aromatic conjugation. These atoms are involved in favorable contacts with the gate keeper valine 555 and with alanine 634, respectively. Interestingly, the latter amino acid is replaced by a cysteine residue in VEGFR2. The increased steric hindrance of cysteine compared to alanine might account for an energy penalty in order for the VEGF receptor to accommodate **1h** in its ATP binding site, thus providing a potential rationale for the selectivity of the compound against this receptor.

More generally, the model suggests that the specificity of **1h** for the FGFR kinases originates in an optimal fit of the dichlorodimethoxy phenyl moiety to the particular shape of the ATP site back pocket observed in the available crystal structures of these enzymes (FGFR1 and FGFR2). This stems from the conjunction of a small valine gate keeper residue, a small alanine residue

preceding the DFG motif (A634 in FGFR3), and a particular rotameric state of the side chain of the phenylalanine residue in the DFG motif (F636 in FGFR3). This unusual side chain conformation having only been observed in the crystal structures of FGFR kinases.

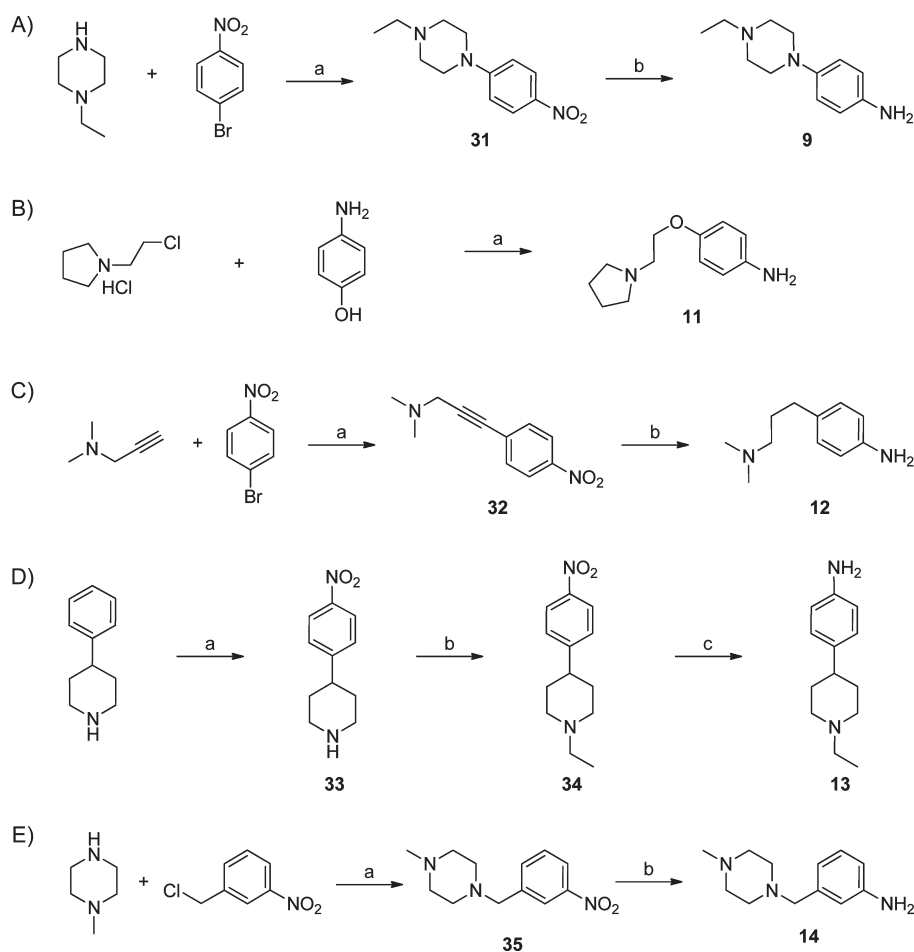
The above binding model could be validated by the determination of the crystal structure of the FGFR1 kinase domain in complex with **1h** at 2.8 Å resolution. All the putative interactions, described in Figure 10, between the inhibitor and the equivalent residues in FGFR1 which are all conserved (as well as in FGFR2 and FGFR4) are indeed observed in this crystal structure. In particular, the speculated water mediated hydrogen bond between the urea carbonyl group of the inhibitor and the side chain of lysine 508 (K514 in FGFR1) exists in the X-ray structure. A representation of the ATP site region of the cocrystal structure is shown in Figure 11.

**Synthesis of Compounds 1a–n.** Compounds **1a–n** were prepared by addition of pyrimidine-4,6-diamines **16–25** to the isocyanates obtained by treatment of anilines **26–30** with phosgene (Scheme 1).

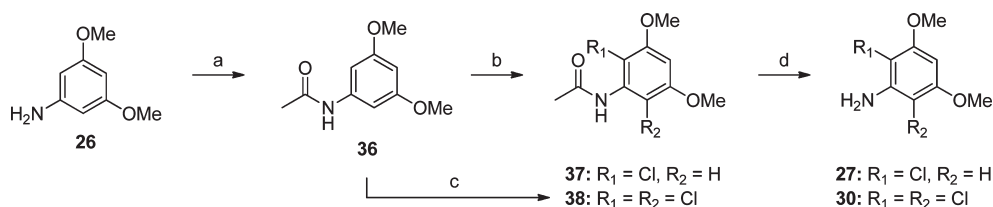
Treatment of 4,6-dichloropyrimidine (**4**) with either aqueous ammonia, ethanolic methylamine, or aqueous ethylamine afforded 4-amino-6-chloropyrimidines **5**, **6**, and **7**, respectively, which underwent subsequent reaction with aniline **8** to provide the corresponding diaminopyrimidines **16**, **17**, and **18**. The pyrimidine-4,6-diamine analogues **19–25** were prepared similarly from compound **6** and amines **9–15**. These reactions were carried out using either aqueous acetic acid or 4 N hydrochloric acid in dioxane, the latter being a convenient alternative to acetic acid when the acetylation of the aniline is predominant to the desired substitution of the chlorine atom. The structures of commercially available anilines **8**, **10**, **15**, and **28** are shown in Figure 12.

Anilines **9**, **11–14** were prepared according to the synthetic routes described in Scheme 2.

With the exception of **11**, these anilines were prepared from the corresponding nitrobenzene precursors. Thus, amine **9** was the product of the Raney nickel-catalyzed hydrogenation of 1-ethyl-4-(4-nitrophenyl)piperazine **31**, obtained by reacting 1-bromo-4-nitrobenzene and 1-ethylpiperazine at 80 °C for 15 h (Scheme 2A). Aniline **11** could instead be synthesized by etherification of 4-aminophenol with 1-(2-chloroethyl)pyrrolidine hydrochloride using finely powdered sodium hydroxide in DMF (Scheme 2B). It is noteworthy that an efficient mechanical stirring of the suspension was critical in order to ensure the

Scheme 2. Synthesis of Anilines 9, 11–14<sup>a</sup>

<sup>a</sup> Reagents and conditions: (A) (a) 80 °C, 15 h (89%); (b) Raney Ni, H<sub>2</sub>, MeOH, 25 °C, 7 h (98%). (B) (a) NaOH, DMF, 75 °C, 2 h (92%). (C) (a) (t-Bu)<sub>3</sub>P, Pd(PhCN)<sub>2</sub>Cl<sub>2</sub>, CuI, dioxane, 25 °C, 22 h (90%); (b) 10% Pd on carbon, H<sub>2</sub>, EtOH, 25 °C, 22 h (68%). (D) (a) H<sub>2</sub>SO<sub>4</sub>, HNO<sub>3</sub>, CH<sub>3</sub>COOH (47%); (b) CH<sub>3</sub>CHO, Na(OAc)<sub>3</sub>BH, CH<sub>2</sub>Cl<sub>2</sub>, 5 °C, 1 h (70%); (c) 10% Pd on carbon, H<sub>2</sub>, EtOH, 25 °C, 3 h (33%). (E) (a) K<sub>2</sub>CO<sub>3</sub>, acetone, reflux, 15 h (100%); (b) Raney Ni, H<sub>2</sub>, MeOH, 25 °C, 5 h (84%).

Scheme 3. Synthesis of Anilines 27 and 30<sup>a</sup>

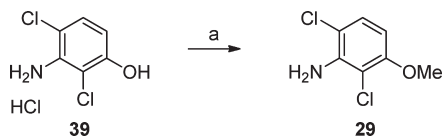
<sup>a</sup> Reagents and conditions: (a) acetic anhydride, toluene, 25 °C (97%); (b) sodium chlorate, acetic acid, 32% HCl (in H<sub>2</sub>O), 0 °C (47%); (c) SO<sub>2</sub>Cl<sub>2</sub>, CH<sub>3</sub>CN, 0 °C (58%); (d) 2 N KOH, ethanol (27, 100%; 30, 92%).

high-yielding formation of the desired product. Scheme 2C illustrates the preparation of aniline 12 by Sonogashira coupling of 3-dimethylamino-1-propyne with 1-bromo-4-nitrobenzene and subsequent hydrogenation of the resulting product (32) in the presence of palladium on carbon. Compound 13 was synthesized according to a three-step protocol involving the nitration of 4-phenylpiperidine, the reductive ethylation of 33, and the catalytic hydrogenation of the corresponding nitro derivative 34 (Scheme 2D). Nitrobenzene 35, derived from the alkylation

of 3-nitrobenzylchloride with 1-methylpiperazine in the presence of potassium carbonate, was reduced to aniline 14 (Scheme 2E) in analogy to the protocol used for the synthesis of amine 9.

The preparation of anilines 27 and 30 was carried out according to a two-step protocol starting from acetamide 36, readily accessible by acetylation of 3,5-dimethoxyaniline (26) (Scheme 3).

The extent of the chlorination of 36 could be modulated by the appropriate selection of the ratio between 36 and the reagent

Scheme 4. Synthesis of Aniline 29<sup>a</sup>

<sup>a</sup> Reagents and conditions: (a) dimethyl sulfate, KOH, acetone, 25 °C (91%).

utilized as the chlorine source. While compound **36** reacted with a substoichiometric amount of sodium chlorate to afford 2-chloro-substituted amide **37**, the use of an excess of sulfuryl chloride provided the 2,6-dichloro analogue (**38**). Conversion of **37** and **38** to the corresponding anilines (**27** and **30**, respectively) was accomplished by hydrolytic deacetylation under basic conditions (Scheme 3).

Aniline **29** was synthesized by treatment of commercially available 2,4-dichloro-3-aminophenol hydrochloride (**39**) with potassium hydroxide in acetone and subsequent methylation with dimethyl sulfate (Scheme 4).

## CONCLUSIONS

Following an original scaffold morphing concept and exploiting crystallographic information, we have identified *N*-aryl-*N'*-pyrimidin-4-yl-urea compounds as a new class of potent and selective FGFR inhibitors. Evaluation of reversible inhibition of a panel of human CYP450 enzymes by the most potent derivatives in this series indicated **1h** as the one exhibiting the least likelihood for drug–drug interactions. Preliminary assessment of the pharmacokinetic properties of **1h** in mice and rats revealed that the compound was orally bioavailable in rodents, thus justifying additional studies to determine its anticancer efficacy in vivo. Compound **1h** potently inhibited the proliferation of bladder cancer cells overexpressing wild-type FGFR3 and demonstrated significant dose-dependent antitumor activity in RT112 bladder cancer xenografts correlating with the inhibition of the pharmacodynamic markers, pFRS2 and pMAPK, in the tumor. These results support further evaluation of this novel inhibitor with the aim to assess its therapeutic potential in those malignancies characterized by FGF/FGFR genetic alterations.

## EXPERIMENTAL SECTION

**Chemistry.** Proton magnetic resonance spectra were recorded on either a Varian Mercury 400 MHz or a Bruker Avance 600 MHz spectrometer. Carbon magnetic resonance spectra were recorded on a Bruker Avance 600 MHz spectrometer. High-resolution mass spectra were recorded on a THERMO LTQ Orbitrap XL mass spectrometer. Column chromatography was performed on Merck silica gel 60 (particle size of 40–63 μm). Analytical high-pressure liquid chromatography (HPLC) analyses were conducted using: (i) a Hewlett-Packard 1100 series system, UV detection at 215 nm; a column Nucleosil 100–3 C18 4 mm × 70 mm, a linear gradient from 20% to 100% A over 5 min and then 100% B for 1.5 min (A = CH<sub>3</sub>CN + 0.1% CF<sub>3</sub>COOH and B = H<sub>2</sub>O + 0.1% CF<sub>3</sub>COOH), flow rate 1 mL/min, temperature 30 °C (HPLC 1); (ii) a Waters system equipped with a CTC Analytics HTS PAL auto-sampler, 515 pumps, UV detection at 210 nm, a column Nucleosil 100–3 C18 3 mm × 70 mm, a linear gradient from 0% to 95% A over 6.6 min and then 95% A for 4.4 min (A = CH<sub>3</sub>CN + 20% H<sub>2</sub>O + 0.1% H<sub>3</sub>PO<sub>4</sub> (85%) + 1% (CH<sub>3</sub>)<sub>4</sub>NOH (10%) and B = H<sub>2</sub>O + 0.2% H<sub>3</sub>PO<sub>4</sub>

(85%) + 2% (CH<sub>3</sub>)<sub>4</sub>NOH (10%)), flow rate 1.2 mL/min, temperature, 45 °C (HPLC 2). Purities for final compounds were measured by analytical HPLC and are ≥95.0%.

**3-(2,6-Dichloro-3,5-dimethoxy-phenyl)-1-{6-[4-(4-ethylpiperazin-1-yl)-phenylamino]-pyrimidin-4-yl}-1-methyl-urea (**1h**): Procedure A.** To a stirred solution of **30** (2.03 g, 9.2 mmol) in dioxane (25 mL) was added 20% phosgene in toluene (8.1 mL, 15.3 mmol), under an argon atmosphere. The resulting mixture was heated to reflux for 1 h, allowed to cool to room temperature, and concentrated in vacuo. The solid residue was added portionwise to a solution of **19** (2.39 g, 7.7 mmol) in toluene (70 mL), under argon. After the end of the addition, the reaction mixture was heated to reflux, stirred for 1.5 h, allowed to cool to room temperature, and diluted with CH<sub>2</sub>Cl<sub>2</sub> and a saturated aqueous solution of NaHCO<sub>3</sub>. The aqueous layer was separated and extracted with CH<sub>2</sub>Cl<sub>2</sub>. The organic phase was washed with brine, dried (Na<sub>2</sub>SO<sub>4</sub>), filtered, and concentrated. Purification of the crude product by silica gel column chromatography (CH<sub>2</sub>Cl<sub>2</sub>/MeOH/aqueous NH<sub>3</sub>, 96:3:1), followed by trituration of the resulting material with MeOH, provided 1.79 g of the desired product (batch 1). Mixed fractions were combined and concentrated. The residue was purified by silica gel column chromatography (CH<sub>2</sub>Cl<sub>2</sub>/MeOH/aqueous NH<sub>3</sub>, 94:5:1), followed by trituration of the resulting material with MeOH, to give additional 1.26 g of pure product (batch 2). The two batches were combined to afford **1h** (3.05 g, 71%) as a colorless solid. HPLC *t*<sub>R</sub> = 3.53 min (HPLC 1). <sup>1</sup>H NMR (600 MHz, DMSO-*d*<sub>6</sub>) δ 1.02 (t, *J* = 7.1 Hz, 3 H), 2.35 (q, *J* = 7.2 Hz, 2 H), 2.41–2.50 (m, 4 H), 3.03–3.12 (m, 4 H), 3.29 (s, 3 H), 3.93 (s, 6 H), 6.39 (s, 1 H), 6.89 (s, 1 H), 6.91 (d, *J* = 9.2 Hz, 2 H), 7.39 (d, *J* = 8.3 Hz, 2 H), 8.37 (s, 1 H), 9.44 (s, 1 H), 12.05 (s, 1 H). <sup>13</sup>C NMR (151 MHz, DMSO-*d*<sub>6</sub>) δ 12.0, 31.7, 48.6 (2 C), 51.6, 52.4 (2 C), 56.7 (2 C), 89.8, 96.6, 112.6 (2 C), 115.8 (2 C), 122.0 (2 C), 134.5, 147.3, 152.8, 154.2 (3 C), 155.9, 159.2, 161.7. HRMS for C<sub>26</sub>H<sub>32</sub>Cl<sub>2</sub>N<sub>7</sub>O<sub>3</sub> (M + H)<sup>+</sup> calcd 560.1937, found 560.1938.

**Preparation of the Monophosphate Salt of Compound 1h.** A suspension of **1h** (134 g, 240 mmol) in 2-propanol (2000 mL) was heated to 50 °C with stirring. To this suspension was added portionwise a solution of phosphoric acid (73.5 g, 750 mmol) in water (2000 mL). The mixture was stirred at 60 °C for 30 min and filtered through a polypropylene pad. The pad was washed with warm 2-propanol/water (1:1, 200 mL). The filtrates were combined to provide a clear solution to which 2-propanol (6000 mL) was added. The resulting mixture was stirred under reflux for 20 min, cooled slowly to room temperature, and stirred for 24 h. The white salt product was collected by filtration, washed with 2-propanol (2 × 500 mL), and dried in the oven at 60 °C under reduced pressure over two days to give the monophosphate salt of compound **1h** (110 g, 70%): Anal. Calcd for C<sub>26</sub>H<sub>34</sub>Cl<sub>2</sub>N<sub>7</sub>O<sub>7</sub>P (658.49): C, 47.42; H, 5.20; Cl, 10.77; N, 14.89; O, 17.01; P, 4.70. Found: C, 47.40; H, 5.11; Cl, 10.73; N, 14.71; O, 17.18; P, 4.87.

**(6-Chloro-pyrimidin-4-yl)-methyl-amine (6).** To a suspension of 4,6-dichloropyrimidine (**4**, 20 g, 132 mmol) in 2-propanol (60 mL) was added 33% methylamine in ethanol (40 mL, 329 mmol) at such a rate that the internal temperature did not rise above 50 °C. After completion of the addition, the reaction mixture was stirred for 1 h at room temperature. Water (50 mL) was added, and the resulting suspension was cooled in an ice bath to 5 °C. The precipitated product was filtered off and washed with cold 2-propanol/water (2:1, 45 mL) and water. The collected material was dried in vacuo at 45 °C overnight to afford **6** (16.2 g, 86%) as colorless powder. HPLC *t*<sub>R</sub> = 3.57 min (HPLC 1). <sup>1</sup>H NMR (400 MHz, CDCl<sub>3</sub>) δ 2.99 (d, *J* = 4.3 Hz, 3 H), 5.31 (br s, 1 H), 6.39 (s, 1 H), 8.38 (s, 1 H). ESI-MS: 144.3 (M + H)<sup>+</sup>.

**4-(4-Ethylpiperazin-1-yl)-phenylamine (9).** A mixture of **31** (6.2 g, 26.35 mmol) and Raney nickel (2 g) in MeOH (120 mL) was stirred for 7 h at room temperature, under a hydrogen atmosphere. The reaction mixture was filtered through a pad of Celite. The filtrate was concentrated to afford **9** (5.3 g, 98%) as a violet solid. <sup>1</sup>H NMR (400 MHz, DMSO-*d*<sub>6</sub>) δ 1.03 (t, *J* = 7.23 Hz, 3 H), 2.37 (q, *J* = 7.3 Hz,

2 H), 2.45–2.55 (m, 4 H), 2.85–2.95 (m, 4 H), 4.59 (br s, 2 H), 6.47–6.53 (m, 2 H), 6.66–6.72 (m, 2 H). ESI-MS: 206.1 (M + H)<sup>+</sup>.

**N-[4-(4-Ethyl-piperazin-1-yl)-phenyl]-N'-methyl-pyrimidine-4,6-diamine (19).** A mixture of **6** (1.81 g, 12.7 mmol) and **9** (2 g, 9.8 mmol) in a mixture of water (4 mL) and glacial acetic acid (20 mL) was heated to 100 °C for 16 h. After further addition of **6** (0.5 g, 3.5 mmol), the reaction mixture was stirred for additional 24 h at 100 °C, cooled, and concentrated. The resulting aqueous residue was made basic by addition of a saturated aqueous solution of NaHCO<sub>3</sub> and extracted with CH<sub>2</sub>Cl<sub>2</sub>. The combined organic extracts were washed with brine, dried (Na<sub>2</sub>SO<sub>4</sub>), filtered, and concentrated. The residue was triturated in ethyl acetate to afford **19** (2.13 g, 70%) as a colorless solid. <sup>1</sup>H NMR (400 MHz, DMSO-*d*<sub>6</sub>) δ 1.05 (t, *J* = 7.23 Hz, 3 H), 2.39 (q, *J* = 7.0 Hz, 2 H), 2.65–2.75 (m, 4 H), 3.05–3.15 (m, 4 H), 3.30–3.35 (m, 3 H), 5.60 (s, 1 H), 6.70 (d, *J* = 4.7 Hz, 1 H), 6.89 (d, *J* = 9.0 Hz, 2 H), 7.31 (d, *J* = 8.6 Hz, 2 H), 8.02 (s, 1 H), 8.60 (br s, 1 H). ESI-MS: 313.2 (M + H)<sup>+</sup>.

**2,6-Dichloro-3,5-dimethoxy-phenylamine (30).** To a solution of **38** (34.5 g, 264 mmol) in ethanol (1300 mL) was added 2 N KOH (720 mL). The reaction mixture was heated to reflux, stirred for 44 h, and allowed to cool to room temperature. The resulting suspension was cooled to 0 °C, stirred for 1 h, and filtered. The residue was washed with a small portion of cold ethanol/water (1:1) and with cold water until neutrality and dried to provide **30** (26.7 g, 92%) as a colorless solid. <sup>1</sup>H NMR (400 MHz, DMSO-*d*<sub>6</sub>) δ 3.85 (s, 6 H), 5.44 (s, 2 H), 6.24 (s, 1 H). ESI-MS: 222.0 (M + H)<sup>+</sup>.

**1-Ethyl-4-(4-nitro-phenyl)-piperazine (31).** A mixture of 1-bromo-4-nitrobenzene (6 g, 29.7 mmol) and 1-ethylpiperazine (7.6 mL, 59.4 mmol) was heated to 80 °C and stirred for 15 h. The reaction mixture was allowed to cool to room temperature and diluted with water and CH<sub>2</sub>Cl<sub>2</sub>/MeOH (9:1). The aqueous layer was separated and extracted with CH<sub>2</sub>Cl<sub>2</sub>/MeOH (9:1). The organic phase was washed with brine, dried (Na<sub>2</sub>SO<sub>4</sub>), filtered, and concentrated. The residue was purified by silica gel column chromatography (CH<sub>2</sub>Cl<sub>2</sub>/MeOH + 1% of aqueous NH<sub>3</sub>, 9:1) to afford **31** (6.2 g, 89%) as a yellow solid: HPLC *t*<sub>R</sub> = 2.35 min (HPLC 1). <sup>1</sup>H NMR (400 MHz, DMSO-*d*<sub>6</sub>) δ 1.05 (t, *J* = 7.2 Hz, 3 H), 2.39 (q, *J* = 7.0 Hz, 2 H), 2.44–2.57 (m, 4 H), 3.45–3.50 (m, 4 H), 7.05 (d, *J* = 9.4 Hz, 2 H), 8.07 (d, *J* = 9.4 Hz, 2 H). ESI-MS: 236.0 (M + H)<sup>+</sup>.

**N-(3,5-Dimethoxy-phenyl)-acetamide (36).** Acetic anhydride (13 mL, 137 mmol, 1.05 equiv) was added in 15 min to a suspension of 3,5-dimethoxyaniline (**26**, 20 g, 131 mmol) in toluene (110 mL), keeping the internal temperature in the range of 35–45 °C. The reaction mixture was allowed to stir for 20 h at room temperature. The resulting thick, gray suspension was diluted with hexane (55 mL) and filtered. The residue in the filter was washed with toluene/hexane (2:1, 70 mL) and hexane and dried to provide **36** (24.8 g, 97%) as a colorless solid. HPLC *t*<sub>R</sub> = 3.03 min (HPLC 1). <sup>1</sup>H NMR (400 MHz, DMSO-*d*<sub>6</sub>) δ 2.03 (s, 3 H), 3.71 (s, 6 H), 6.21 (t, *J* = 2.1 Hz, 1 H), 6.84 (d, *J* = 2.3 Hz, 2 H), 9.89 (s, 1 H). ESI-MS: 196.0 (M + H)<sup>+</sup>.

**N-(2,6-Dichloro-3,5-dimethoxy-phenyl)-acetamide (38).** Sulfuryl chloride (26.9 mL, 325 mmol) was added in 7 min to a cold (0 °C) suspension of **36** (32.9 g, 169 mmol) in CH<sub>3</sub>CN (500 mL), under an argon atmosphere. The resulting yellowish mixture was allowed to stir for 30 min and quenched by dropwise addition of a saturated aqueous solution of NaHCO<sub>3</sub> (250 mL). The resulting precipitate was collected by vacuum filtration, washed with H<sub>2</sub>O (300 mL), and dried to afford 20 g of the desired product (batch 1). The filtrate was diluted with a saturated aqueous solution of NaHCO<sub>3</sub> (300 mL) and extracted with ethyl acetate (2 × 300 mL). The organic phase was washed with H<sub>2</sub>O and brine, dried (Na<sub>2</sub>SO<sub>4</sub>), filtered, and concentrated. The residue is purified by silica gel column chromatography (ethyl acetate/hexanes, 1:1 → 2:1) to provide 8.8 g of product (batch 2). Batch 1 and 2 were combined and stirred in hexane. The solid was collected by filtration, washed with hexane, and dried to afford **38** (25.8 g, 58%) as a colorless solid. <sup>1</sup>H NMR (400 MHz, DMSO-*d*<sub>6</sub>)

δ 2.05 (s, 3 H), 3.94 (s, 6 H), 6.90 (s, 1 H), 9.76 (s, 1 H). ESI-MS: 264.0 (M + H)<sup>+</sup>.

**Radiometric Kinase Assay.** The enzymatic kinase activity was assessed by measuring the phosphorylation of a synthetic substrate by the purified GST-fusion FGFR3-K650E kinase domain, in the presence of radiolabeled ATP. Enzyme activities were measured by mixing 10 μL of a 3-fold concentrated compound solution or control with 10 μL of the corresponding substrate mixture (peptidic substrate, ATP and [<sup>33</sup>P]ATP). The reactions were initiated by addition of 10 μL of a 3-fold concentrated solution of the enzyme in assay buffer. The final concentrations of the assay components were as following: 10 ng of GST-FGFR3-K650E, 20 mM Tris-HCl, pH 7.5, 3 mM MnCl<sub>2</sub>, 3 mM MgCl<sub>2</sub>, 1 mM DTT, 250 μg/mL PEG 20000, 2 μg/mL poly(EY) 4:1, 1% DMSO and 0.5 μM ATP (γ-<sup>33</sup>P]-ATP 0.1 μCi). The assay was carried out according to the filter binding (FB) method in 96-well plates at room temperature for 10 min in a final volume of 30 μL including the components as indicated above. The enzymatic reactions were stopped by the addition of 20 μL of 125 mM EDTA, and the incorporation of <sup>33</sup>P into the polypeptidic substrates was quantified as following: 30 μL of the stopped reaction mixture were transferred onto Immobilon-PVDF membranes previously soaked for 5 min with methanol, rinsed with water, soaked for 5 min with 0.5% H<sub>3</sub>PO<sub>4</sub>, and mounted on vacuum manifold with disconnected vacuum source. After spotting, vacuum was connected, and each well rinsed with 0.5% H<sub>3</sub>PO<sub>4</sub> (200 μL). Free membranes were removed and washed four times on a shaker with 1% H<sub>3</sub>PO<sub>4</sub> and once with ethanol. Membranes were dried and overlaid with addition of 10 μL/well of a scintillation fluid. The plates were eventually sealed and counted in a microplate scintillation counter. IC<sub>50</sub> values were calculated by linear regression analysis of the percentage inhibition of the compound.

**BaF3 Cell Lines Proliferation Assays.** Murine BaF3 cell lines, whose proliferation and survival has been rendered IL-3-independent by stable transduction with tyrosine kinases activated either by mutation or fusion with a dimerizing partner, were cultured in RPMI-1640 media (Gibco Cat. no. 11875093, Carlsbad, CA) supplemented with 10% FBS (Hyclone Cat no. SV30014.03, Logan, UT), 4.5 g/L glucose (Sigma no. G5400, St. Louis, MO), 1.5 g/L sodium bicarbonate (Biowhittaker no. 17–613E, Walkersville, MD), and Pen/Strep (Gibco no. 10378–016, Carlsbad, CA). Cells were passaged twice weekly. Compound-mediated inhibition of BaF3 cell proliferation and viability was assessed using a Luciferase bioluminescent assay (Bright-Glo, Promega, Madison, WI, USA). Exponentially growing BaF3 or BaF3 Tel-TK cells were seeded into 384-well plates (4250 cells/well) at 50 μL/well using a μFill liquid dispenser (BioTek, Winooski, VT, USA) in fresh medium. Compound **1h** was serially diluted in DMSO and arrayed in a polypropylene 384-well plate. Then 50 nL of compound were transferred into the plates containing the cells by using the pintool transfer device, and the plates incubated at 37 °C (5% CO<sub>2</sub>) for 48 h. Then 25 μL of Bright-Glo were added, and luminescence was quantified using an Analyst-GT (Molecular Devices, Sunnyvale, CA, USA). Custom curve-fitting software was used to produce a logistic fit of percent cell viability as a function of the logarithm of inhibitor concentration. The IC<sub>50</sub> value was determined as the concentration of compound needed to reduce cell viability to 50% of a DMSO control.

**FGFR1–4 Cellular Autophosphorylation Assays.** HEK293 cells seeded in 96-well plates were transiently transfected with pcDNA3.1 vectors encoding for FGFR1, FGFR2, FGFR3-K650E, FGFR3-S249C, FGFR4, or pcDNA3.1 empty vector using Fugene-6 reagent (Roche no. 11814443001). At 24 h post-transfection, cells were treated in triplicates with serial dilutions of the compound, prepared in DMSO, or DMSO for 40 min at 37 °C. The final concentration of DMSO in the cells was 0.2%. Cells were lysed in 100 μL/well of lysis buffer (50 mM Tris pH 7.5, 150 mM NaCl, 1 mM EGTA, 5 mM EDTA, 1% Triton, 2 mM NaVanadate, 1 mM PMSF, and protease inhibitors cocktail Roche

no. 11873580001), and 50  $\mu\text{L}$  of cell lysate were transferred to the FluoroNunc plates coated with FGFR capturing antibodies ( $\alpha$ -FGFR1 antibody: R&D Systems no. MAB766;  $\alpha$ -FGFR2 antibody, R&D Systems no. MAB665;  $\alpha$ -FGFR3 antibody, R&D Systems no. MAB766;  $\alpha$ -FGFR4 antibody, R&D Systems no. MAB685). Capturing was allowed to proceed for 5 h at 4  $^{\circ}\text{C}$ . The plate was washed with PBS/O containing 0.05% Tween.  $\alpha$ -pTyr-antibody coupled to alkaline phosphates (Zymed PY20 no. 03–7722) was added overnight at 4  $^{\circ}\text{C}$ . The signal was revealed by adding CDP-Star substrate (Applied Biosystems no. MS1000RY) for 45 min, and the luminescence was next measured using TOP Count NXT luminometer (Packard Bioscience). The inhibitory activity of the compound was calculated as the percentage of the DMSO-treated samples, and  $\text{IC}_{50}$  values were determined as the concentration of compound needed to inhibit the signal by 50%.

**Bladder Cancer Cell lines Proliferation Assays.** Bladder cancer cell lines were obtained either from ATCC or DSMZ. Bladder cancer cell proliferation was measured in 96-well plates. 8500 cells/well (RT4, RT112) or 5000 cells/well (J82, HT1197, VMCUB1, JMSU1, SW780, UMUC3) were seeded in a volume of 100  $\mu\text{L}$ /well in growth media. Media containing compound dilutions or DMSO was added 24 h thereafter. After 72 h, cells were fixed by addition of 25  $\mu\text{L}$ /well glutaraldehyde (20%) for 10 min at room temperature. Cells were washed twice with 200  $\mu\text{L}$ /well  $\text{H}_2\text{O}$ , and 100  $\mu\text{L}$  of Methylene Blue (0.05%) were added. After incubation for 10 min at room temperature, cells were washed three times with 200  $\mu\text{L}$ /well  $\text{H}_2\text{O}$ . Upon addition of 200  $\mu\text{L}$ /well HCl (3%) and incubation for 30 min at room temperature on a plate shaker, OD650 nm was measured. The concentration of compound providing 50% of proliferation inhibition was calculated using Excel Fit.

**Cytochrome P450 Assay.** Six probe substrates, each specific for a particular CYP450, were used as follows: 7-benzoyloxy-4-(trifluoromethyl)-coumarin (CYP3A4), dibenzylfluorescein (CYP3A4), 7-methoxy-4-trifluoromethylcoumarin (CYP2C9), 3-cyano-7-ethoxycoumarin (CYP2C19, CYP1A2), and 3-[2-(*N,N*-diethyl-*N*-methylamino)ethyl]-7-methoxy-4-methylcoumarin (CYP2D6). Assays were conducted at 37  $^{\circ}\text{C}$  in the presence of a NADPH regenerating system using a 384-well format. Probe substrate metabolites were quantified by fluorescence detection. The  $\text{IC}_{50}$  values were determined using ExcelFit curve-fitting software.

**Pharmacokinetic Parameters in Rodents.** The pharmacokinetic properties of compound **1h** were determined in RT112/luc1-tumor bearing mice. The parental RT112 cell line was stably infected with a retrovirus that constitutively expresses luciferase (pLNCX2/luc1) to generate RT112/luc1 cells. RT112/luc1 tumors were established by subcutaneous injection of  $5 \times 10^6$  cells in 100  $\mu\text{L}$  of HBSS (Sigma no. H8264) containing 50% Matrigel (BD no. 356234) into the right flank of female HsdNpa:Athymic Nude-nu mice. Appropriately sized tumors (ca. 300–400  $\text{mm}^3$ ) developed 20–26 days following cell injection.

Compound **1h** was administered either as a solution in NMP/PEG200 (1:9, v/v) by tail vein injection (5 mg/kg) or as a suspension in PEG300/D5W (2:1, v/v) by oral gavage (20 mg/kg). At the allotted times (0.083, 0.25, 0.5, 1, 2, 6, 8, 24 h), the groups of mice ( $n = 4$ ) were sacrificed, blood and tumors removed, extracted, and the concentration of compound determined by high pressure liquid chromatography/tandem mass spectrometry (LC-MS/MS) using the positive electrospray mode. Limit of quantification (LOQ) for plasma and tumors was set to 5 ng/mL and 10 ng/g, respectively. Relevant pharmacokinetic parameters were derived by noncompartmental analysis (WinNonlin version 4.0, Pharsight). Area under the concentration versus time curve (AUC) was calculated by linear trapezoidal rule.

The pharmacokinetic properties of **1h** in rats were determined as follows. The compound was administered intravenously to the femoral vein of female Wistar rats as a solution in NMP/PEG200 (1:9, v/v) at 5 mg/kg. The monophosphate salt of compound **1h** was administered as a solution in acetic acid–acetate buffer pH 4.6/PEG300 at 10 mg/kg. Dosing with the salt forms was based on free base equivalents. Serial

plasma samples were collected by sublingual vein bleeding for 24 h (0.083, 0.25, 0.5, 1, 2, 6, 8, 24 h) either from two separate groups of rats ( $n = 4$ ), using a staggered sampling design, or by sequential bleeding of one group ( $n = 3$ –4). Samples were extracted and the concentration of compound determined by LC-MS/MS. Pharmacokinetic parameters were derived in analogy to the method described above. LOQ was set to 10 ng/mL.

**In Vivo Antitumor Activity in Mouse Model.** Female HsdNpa:Athymic Nude-nu mice were obtained from Laboratory Animal Services, Novartis Pharma AG, Basel. The animals were kept under optimized hygienic conditions (OHC) in Makrolon type III cages (maximum of 10 animals/cage) and were provided with food and water ad libitum.

The parental RT112 cell line was stably infected with the retroviral vector pLNCX2/luc1. Each mouse was inoculated with approximately 25–50  $\mu\text{L}$  of cell suspension ( $\sim 1$ – $2 \times 10^5$  cells) directly in the bladder lumen. Tumor growth measurements were done by noninvasive imaging using a Xenogen IVIS imaging system. Measurements were performed 10 min after intravenous injection of 10 mL/kg (50 mg/mL in PBS) D-luciferin.

Compound **1h** was formulated as a suspension in PEG300/D5W (2:1, v/v) and administered orally for 12 consecutive days at the doses of 10 and 30 mg/kg/qd. Tumor and body weight data were analyzed by ANOVA with post hoc Dunnett's test for comparison of treatment versus control group. The post hoc Tukey test was used for intragroup comparison. Statistical analysis was performed using GraphPad prism 4.02 (GraphPad Software). As a measure of efficacy, the  $T/C$  (%) value was calculated at a certain number of days after treatment start according to:

$$\left( \Delta \text{light emission}^{\text{treated}} / \Delta \text{light emission}^{\text{control}} \right) \times 100$$

$\Delta$  light emission represents the mean light emission on the evaluation day minus the mean light emission at the start of the experiment.

**In Vivo Antitumor Activity in Rat Model.** Female nude Rowlett rats 6–9 weeks of age were obtained from Harlan (The Netherlands). The animals were kept under optimized hygienic conditions (OHC) in Makrolon type III cages (maximum of 2 animals per cage) and were provided with food and water ad libitum. RT112 tumors were established by subcutaneous injection of  $1 \times 10^6$  cells in 100  $\mu\text{L}$  of HBSS containing 50% Matrigel into the right flank of nude rats. Treatments were initiated when the mean tumor volumes were approximately 100  $\text{mm}^3$ . The monophosphate salt of compound **1h** was formulated as a solution in acetic acid–acetate buffer pH 4.6/PEG300 (1:1, v/v) and applied daily by gavage to the tumor-bearing rats ( $n = 8$ ) for 20 consecutive days at doses of 5, 10, and 15 mg/kg/qd (free base equivalents). The application volume was 5 mL/kg.

Tumor volumes were measured with calipers and determined according to the formula: length  $\times$  width  $\times$  height  $\times \pi/6$ .

Antitumor activity was expressed as  $T/C$  (%): (mean change of tumor volume of treated animals/mean change of tumor volume of control animals)  $\times 100$ .

Regressions (%) were calculated according to the formula: [(mean tumor volume at end of treatment – mean tumor volume at start of treatment)/mean tumor volume at start of treatment]  $\times 100$ .

In the pharmacodynamic study, RT112 tumor-bearing rats ( $n = 4$ ) received a single oral administration of the monophosphate salt of compound **1h**, formulated as described above, at the doses of 4.25 and 8.51 mg/kg (free base equivalents). Tumors were collected at various time points post-therapy, frozen, minced, and homogenized in an equal volume of ice-cold phosphate buffered saline (PBS) using a Polytron homogenizer (TP18–10, IKA, Staufen, Germany), keeping the material cold during the homogenization. Concentrations of **1h** in tumors were determined by LC-MS/MS. LOQ was set to 3 ng/mL. Aliquots of tumor powder were weighted (50 mg) and resuspended immediately in a ratio of 1:10 (w/v) of ice-chilled lysis buffer containing 50 mM Tris pH 7.5,

150 mM NaCl, 1 mM EGTA, 5 mM EDTA, 1% Triton, 2 mM NaVanadate, 1 mM PMSF, and protease inhibitors cocktail Roche no. 11873580001). Lysates were clarified by centrifugation at 12000g for 15 min, and protein concentration was determined using the DC protein assay reagents (Bio Rad no. 500–0116) and a BSA standard. Total cell lysates were subjected to SDS-PAGE, and proteins were blotted onto PVDF membranes. Filters were blocked in 5% BSA and further incubated with the primary antibodies (pFRS2(Tyr196), Cell Signaling no. 3864; pMAPK, Cell Signaling no. 9101;  $\beta$ -tubulin, Sigma no. T4026) overnight at 40 °C. Proteins were visualized with peroxidase-coupled antimouse or antirabbit AB using the SuperSignalWest Dura Extended Duration Substrate Detection System (Pierce no. 34075).

**In Vivo Antiangiogenic Activity in VEGF/bFGF Agar Chamber Model.** Female FVB mice were implanted with sterile tissue chambers made of perfluoro-alkoxy-Teflon (21 mm  $\times$  8 mm diameter, with 80 regularly spaced 0.8 mm perforations) filled with 500  $\mu$ L of molten 0.8% w/v agar containing 20 U/mL heparin and with or without growth factor (dog VEGF 2  $\mu$ g/mL or bFGF 0.3  $\mu$ g/mL). Compound **1h** was administered orally in doses of 10, 30, and 50 mg/kg daily in a vehicle of 10% NMP in PEG300 (dose volume 5 mL/kg). Treatment was started 4–6 h before implantation of the chambers and continued for 3 days. The implants were removed 24 h after the last dose. The angiogenic response was quantified by measuring the weight and the receptor tyrosine kinase Tie-2 levels of the vascularized tissue grown around the chamber (capsule). Tie-2 measurements were performed by an ELISA assay utilizing the capture antibody anti-Tie-2 AB33. The percentage inhibition of the angiogenic response (increase in capsule weight or total Tie-2) was calculated in individual animals as follows:

$$(A)/(B - C) \times 100$$

A = capsule weight or total Tie-2 from a drug-treated mouse with a chamber containing growth factor.

B = capsule weight or total Tie-2 from the group of vehicle-treated mice with chambers containing growth factor.

C = mean background capsule weight or total Tie-2 from the group of vehicle-treated mice with chambers not containing growth factor.

The statistical comparisons between groups (compound-treated versus nontreated animals) were made using the absolute values for capsule weight and Tie-2 levels (Rank Sums Test, JANDEL SigmaStat 2.0). The significance level was set at  $p < 0.05$ .

**Conformational Calculations.** The initial conformations of the compounds were generated in MacroModel<sup>55</sup> and minimized by molecular mechanics using the AMBER\*/H<sub>2</sub>O/GBSA force field. The ab initio calculations were performed in the Jaguar module of Maestro (Schrödinger Inc., New York, NY, USA) The quantum mechanics method used was DFT(b3lyp) with the 6-31G\*\*+ basis set and the Poisson–Boltzmann method for water solvation energy calculations. The lowest energy molecular mechanics minimized conformations of the compounds were input in Jaguar and were fully minimized without constraints applying the water solvation model. This gave the reference energy of the isolated compound. For each compound, a second minimization was performed constraining the torsion angle defining the orientation of the dimethoxy-phenyl moiety with respect to the plane of the core structure to adopt the value of 110° observed in the FGFR1–compound **3** cocrystal structure. The difference in energy obtained from these two calculations gave an estimate of the deconjugation energy penalty paid by the compound for binding to the kinase.

**Homology Model.** The sequence of the human FGFR3 kinase was obtained from SWISS-PROT,<sup>56</sup> entry P22607. The crystallographic structure of the FGFR1 kinase in complex with compound **3** (PDB code 2FGI from the Protein Data Bank) was chosen as template. The sequences were aligned using T-Coffe.<sup>57</sup> On the basis of the resulting alignment, the 3D structure of the FGFR3 kinase was modeled using the

What If program<sup>58</sup> with the default parameters (PIRPSQ module, BLDPIR command). It should be noted that aside from one residue, A559 (FGFR3), pointing toward the exterior of the pocket, FGFR1 and FGFR3 have identical residues in their ATP binding sites. Thus, we considered the FGFR3 homology model as reliable for docking compounds in the ATP pocket.

**Docking.** Using MacroModel,<sup>55</sup> the inhibitors were constructed, manually docked in the ATP binding site of the FGFR3 kinases model (assuming the same binding mode as that of compound **3** in the FGFR1 crystal structure), and the resulting ligand–protein complexes energy-minimized (AMBER\*/H<sub>2</sub>O/GBSA force field).

**Purification, Crystallization, and Structure of the FGFR1–Compound **1h** Complex.** Human FGFR1 protein was expressed in TN5 insect cells using a construct with an N-terminal His-tag, a spacer, and a TEV cleavage site (comprising a sequence of MGYYHHHHHH-DYDIPTT-ENLYFQG–) followed by amino acids 456–765 of FGFR1; potentially reactive Cys residues were removed from the construct by incorporating two point mutations: C488A and C584S. The cell pellet was lysed using JPER, and the soluble lysate was obtained after centrifugation and removal of cell debris. A 5 mL IMAC column was equilibrated with buffer A (20 mM Tris-HCl, pH 7.5, 150 mM NaCl, 5% (v/v) glycerol, 10 mM imidazole, 5 mM  $\beta$ -mercaptoethanol, 1 tablet of EDTA-free complete protease inhibitor cocktail (Roche), 10  $\mu$ g/mL leupeptin), the cell lysate was loaded onto the column, and the column was washed with buffer until an A280 baseline was reached. The bound protein was then eluted by instituting a gradient where the buffer A imidazole concentration was slowly increased to 250 mM (hereafter, buffer B) during which 5 mL fractions were collected. IMAC fractions were selected for pooling by SDS-PAGE analysis. EDTA was added to pooled IMAC fractions to a final concentration of 1 mM. The pooled IMAC fractions were concentrated to a volume and loaded onto a SEC Superdex 200 2660 column, and the protein was eluted with buffer B while 10 mL fractions were collected. The fractions were selected by SDS-PAGE and pooled. The pooled fractions were diluted with two volumes of buffer C (20 mM Tris-HCl, pH 7.5, 5% (v/v) glycerol, and 5 mM DTT). A 5 mL QHP column was equilibrated with buffer C supplemented with 50 mM NaCl, the pooled fractions were loaded onto the column, and the column was washed. The protein was then eluted using a gradient where the NaCl concentration was gradually increased to a final concentration of 1 M NaCl while 10 mL fractions were collected. The fractions were analyzed by SDS-PAGE and mass spectrometry and pooled. The His-tag was removed by TEV protease digestion overnight at 4 °C. A second IMAC column was run as delineated previously to remove cleaved His-tag and TEV protease, and fractions were analyzed by SDS-PAGE and pooled. The pooled fractions were dialyzed against 2 L of buffer D (20 mM Tris-HCl, pH 7.5, 150 mM NaCl, 5% (v/v) glycerol, 5 mM dithiothreitol, and 0.5 mM EDTA) overnight at 4 °C. The protein was concentrated to approximately 10 mg/mL.

Prior to crystallization, the protein was spun at 10000 rpm in a microfuge at 4 °C for 15 min. The protein was crystallized by the hanging drop vapor diffusion method: 1  $\mu$ L of protein solution was mixed with 1  $\mu$ L of mother liquor, which consisted of a grid of 18–28% (v/v) PEG-MME 5000 with 0.2 M ammonium sulfate and 0.1 M sodium cacodylate. The resulting drop was suspended over a reservoir of 0.5 mL of mother liquor and sealed with vacuum grease. The apo-crystals grew at 4 °C. The FGFR1–**1h** costructure was obtained by a soaking protocol where apo-crystals of FGFR1 were transferred into a large drop of mother liquor supplemented with 2 mM of compound **1h** and stored overnight at 4 °C. Crystals were transferred into a cryoprotectant consisting of mother liquor supplemented with 2 mM of **1h** and 25% (v/v) of glycerol. Crystals were then cryocooled in liquid nitrogen for data collection.

The X-ray diffraction data was collected at Stanford Synchrotron Research Laboratory. Data integration and scaling were performed by

using the programs MOSFLM and SCALA.<sup>59</sup> Data were reduced in the C2 space group, with unit cell dimensions  $a = 209.11 \text{ \AA}$ ,  $b = 50.60 \text{ \AA}$ ,  $c = 66.90 \text{ \AA}$ , and  $\beta = 104.7^\circ$ . There are two monomers in the asymmetric unit. The data set is 99.2% complete in the resolution range of 100.0–2.8  $\text{\AA}$  and has an  $R_{\text{merge}}$  of 15.1% with a multiplicity of 3.4; approximately 6% of the data was flagged for cross-validation of the refinement via the calculation of an  $R_{\text{free}}$  factor. The costructure was determined using molecular replacement with an apo-structure of FGFR1 as the search model. The structure was refined by executing several iterations of manual rebuilding after inspection of  $2F_o - F_c$  and  $F_o - F_c$  difference maps followed by refinement by the program AUTOBUSTER.<sup>60</sup> Data from a resolution range of 25.92–2.8  $\text{\AA}$  was used in the refinement. Refinement parameter files for compound **1h** were generated by the program AFITT (Openeye Scientific Software). The final structure has an  $R$ -factor of 20.41% and an  $R_{\text{free}}$  factor of 26.07%.

The active site and compound **1h** are well-represented in the electron density contoured at  $1\sigma$ , as are adjacent structural waters. The density for the ethyl piperazine group of **1h** is only approximately represented in density, suggesting that it is flexible and/or oscillating, leading to a disordering of the electron density in this region and the adoption of a high-energy conformer for this group during refinement. A low-energy conformation for the ethyl piperazine group was modeled in by hand after the end of the refinement procedure.

## ■ ASSOCIATED CONTENT

**S** Supporting Information. Experimental details (including analytical data) for the final compounds **1a–g**, **1i–n**, and intermediates **5**, **7**, **11–14**, **16–18**, **20–25**, **27**, **29**, **32–35**, **37**; complete data set of Tables 4–5. This material is available free of charge via the Internet at <http://pubs.acs.org>.

## ■ AUTHOR INFORMATION

### Corresponding Author

\*For V.G.: phone, 41 61 696 24 60; fax, 41 61 696 24 55; E-mail, [vito.guagnano@novartis.com](mailto:vito.guagnano@novartis.com). For D.G.P.: phone, 41 61 696 50 93; fax, 41 61 696 70 96; E-mail, [diana.graus\\_porta@novartis.com](mailto:diana.graus_porta@novartis.com).

### Present Addresses

<sup>†</sup>Genentech, Inc., South San Francisco, CA, United States

<sup>‡</sup>Novartis Pharma AG, CH-4002 Basel, Switzerland

<sup>§</sup>Novartis Institute for BioMedical Research, Emeryville, CA, United States

## ■ ACKNOWLEDGMENT

We thank the Novartis Analytical Science Department, Juergen Koeppler, Sandra Molle, Timothy Smith, Wei Gao, Kelly Yan, Wei Shu, the Oncology Protein Sciences Group for technical support, and Robin Fairhurst for proofreading the manuscript.

## ■ ABBREVIATIONS USED

ABL, Abelson; ATP, adenosine triphosphate; AUC, area under the curve; BCR-ABL, breakpoint cluster region–Abelson; BSA, bovine serum albumin; Ci, curie; CL, clearance; D5W, 5% glucose in water; DTT, dithiothreitol; EDTA, ethylenediaminetetraacetic acid; EGTA, ethylene glycol tetraacetic acid; FBS, fetal bovine serum; FGF, fibroblast growth factor; FGFR, fibroblast growth factor receptor; FRS2, fibroblast growth factor receptor substrate 2; GST, glutathione S-transferase; HBSS, Hank's Balanced Salt Solution; HER2, human epidermal growth factor receptor 2; HRMS, high-resolution mass spectra; LCK, lymphocyte-specific protein tyrosine

kinase; LOQ, limit of quantification; MAPK, mitogen-activated protein kinase; MPD, myeloproliferative disorder; NMP, N-methyl-2-pyrrolidinone; PD, pharmacodynamic; PEG, polyethylene glycol; PEG-MME, polyethylene glycol monomethyl ether; PMSF, phenylmethanesulfonyl fluoride; PVDF, polyvinylidene fluoride; qd, quaque die (daily); RTK, receptor tyrosine kinase; SDS-PAGE, sodium dodecyl sulfate polyacrylamide gel electrophoresis; SEM, standard error of mean; TEV, tobacco etch virus; TK, tyrosine kinase; Tris, tris(hydroxymethyl)aminomethane; VEGFR2, vascular endothelial growth factor receptor 2;  $V_{\text{ss}}$ , volume of distribution at steady state; WT, wild-type

## ■ REFERENCES

- (1) Beenken, A.; Mohammadi, M. The FGF family: biology, pathophysiology and therapy. *Nature Rev. Drug Discovery* **2009**, *8*, 235–253.
- (2) Turner, N.; Grose, R. Fibroblast growth factor signalling: from development to cancer. *Nature Rev. Cancer* **2010**, *10*, 116–129.
- (3) Walz, C.; Chase, A.; Schoch, C.; Weisser, A.; Schlegel, F.; Hochhaus, A.; Fuchs, R.; Schmitt-Graeff, A.; Hehlmann, R.; Cross, N. C. P.; Reiter, A. The t(8;17)(p11;q23) in the 8p11 myeloproliferative syndrome fuses MYO18A to FGFR1. *Leukemia* **2005**, *19*, 1005–1009.
- (4) Belloni, E.; Trubia, M.; Gasparini, P.; Micucci, C.; Tapinassi, C.; Confalonieri, S.; Nuciforo, P.; Martino, B.; Lo-Coco, F.; Pelicci, P. G.; Di Fiore, P. P. 8p11 myeloproliferative syndrome with a novel t(7;8) translocation leading to fusion of the FGFR1 and TIF1 genes. *Genes Chromosomes Cancer* **2005**, *42*, 320–325.
- (5) Roumiantsev, S.; Krause, D. S.; Neumann, C. A.; Dimitri, C. A.; Asiedu, F.; Cross, N. C. P.; Van Etten, R. A. Distinct stem cell myeloproliferative/T lymphoma syndromes induced by ZNF198-FGFR1 and BCR-FGFR1 fusion genes from 8p11 translocations. *Cancer Cell* **2004**, *5*, 287–298.
- (6) Grand, E. K.; Grand, F. H.; Chase, A. J.; Ross, F. M.; Corcoran, M. M.; Oscier, D. G.; Cross, N. C. P. Identification of a novel gene, FGFR10P2, fused to FGFR1 in 8p11 myeloproliferative syndrome. *Genes Chromosomes Cancer* **2004**, *40*, 78–83.
- (7) Sohal, J.; Chase, A.; Mould, S.; Corcoran, M.; Oscier, D.; Iqbal, S.; Parker, S.; Welborn, J.; Harris, R. I.; Martinelli, G.; Montefusco, V.; Sinclair, P.; Wilkins, B. S.; Van Den Berg, H.; Vanstraelen, D.; Goldman, J. M.; Cross, N. C. P. Identification of four new translocations involving FGFR1 in myeloid disorders. *Genes Chromosomes Cancer* **2001**, *32*, 155–163.
- (8) Popovici, C.; Adelaide, J.; Ollendorff, V.; Chaffanet, M.; Guasch, G.; Jacrot, M.; Leroux, D.; Birnbaum, D.; Pebusque, M.-J. Fibroblast growth factor receptor 1 is fused to FIM in stem-cell myeloproliferative disorder with t(8;13)(p12;q12). *Proc. Natl. Acad. Sci. U.S.A.* **1998**, *95*, 5712–5717.
- (9) Regenass, U.; Caravatti, G.; Fredenhagen, A.; Wacker, O. Patent WO9532975, 1995.
- (10) Chen, J.; DeAngelo, D. J.; Kutok, J. L.; Williams, I. R.; Lee, B. H.; Wadleigh, M.; Duclos, N.; Cohen, S.; Adelsperger, J.; Okabe, R.; Coburn, A.; Galinsky, I.; Huntly, B.; Cohen, P. S.; Meyer, T.; Fabbro, D.; Roesel, J.; Banerji, L.; Griffin, J. D.; Xiao, S.; Fletcher, J. A.; Stone, R. M.; Gilliland, D. G. PKC412 inhibits the zinc finger 198-fibroblast growth factor receptor 1 fusion tyrosine kinase and is active in treatment of stem cell myeloproliferative disorder. *Proc. Natl. Acad. Sci. U.S.A.* **2004**, *101*, 14479–14484.
- (11) Yagasaki, F.; Wakao, D.; Yokoyama, Y.; Uchida, Y.; Murohashi, I.; Kayano, H.; Taniwaki, M.; Matsuda, A.; Bessho, M. Fusion of ETV6 to fibroblast growth factor receptor 3 in peripheral T-cell lymphoma with a t(4;12)(p16;p13) chromosomal translocation. *Cancer Res.* **2001**, *61*, 8371–8374.
- (12) Chesi, M.; Nardini, E.; Brents, L. A.; Schrock, E.; Ried, T.; Kuehl, W. M.; Bergsagel, P. L. Frequent translocation t(4;14)(p16.3;q32.3) in multiple myeloma is associated with increased expression and activating mutations of fibroblast growth factor receptor 3. *Nature Genet.* **1997**, *16*, 260–264.

- (13) Richelda, R.; Ronchetti, D.; Baldini, L.; Cro, L.; Viggiano, L.; Marzella, R.; Rocchi, M.; Otsuki, T.; Lombardi, L.; Maiolo, A. T.; Neri, A. A novel chromosomal translocation t(4;14)(p16.3;q32) in multiple myeloma involves the fibroblast growth-factor receptor 3 gene. *Blood* **1997**, *90*, 4062–4070.
- (14) Intini, D.; Baldini, L.; Fabris, S.; Lombardi, L.; Ciceri, G.; Maiolo, A. T.; Neri, A. Analysis of FGFR3 gene mutations in multiple myeloma patients with t(4;14). *Br. J. Haematol.* **2001**, *114*, 362–364.
- (15) Cappellen, D.; De Oliveira, C.; Ricol, D.; De Medina, S. G. D.; Bourdin, J.; Sastre-Garau, X.; Chopin, D.; Thiery, J. P.; Radvanyi, F. Frequent activating mutations of FGFR3 in human bladder and cervix carcinomas. *Nature Genet.* **1999**, *23*, 18–20.
- (16) Billerey, C.; Chopin, D.; Aubriot-Lorton, M.-H.; Ricol, D.; Gil Diez de Medina, S.; Van Rhijn, B.; Bralet, M.-P.; Lefrere-Belda, M.-A.; Lahaye, J.-B.; Abbou, C. C.; Bonaventure, J.; Zafrani, E. S.; Van Der Kwast, T.; Thiery, J. P.; Radvanyi, F. Frequent FGFR3 mutations in papillary non-invasive bladder (pTa) tumors. *Am. J. Pathol.* **2001**, *158*, 1955–1959.
- (17) Gomez-Roman, J. J.; Saenz, P.; Cuevas Gonzalez, J.; Escuredo, K.; Santa Cruz, S.; Junquera, C.; Simon, L.; Martinez, A.; Gutierrez Banos, J. L.; Lopez-Brea, M.; Esparza, C.; Val-Bernal, J. F. Fibroblast growth factor receptor 3 is overexpressed in urinary tract carcinomas and modulates the neoplastic cell growth. *Clin. Cancer Res.* **2005**, *11*, 459–465.
- (18) Jang, J. H.; Shin, K. H.; Park, J. G. Mutations in fibroblast growth factor receptor 2 and fibroblast growth factor receptor 3 genes associated with human gastric and colorectal cancers. *Cancer Res.* **2001**, *61*, 3541–3543.
- (19) Takeda, M.; Arao, T.; Yokote, H.; Komatsu, T.; Yanagihara, K.; Sasaki, H.; Yamada, Y.; Tamura, T.; Fukuoka, K.; Kimura, H.; Saijo, N.; Nishio, K. AZD2171 shows potent antitumor activity against gastric cancer over-expressing fibroblast growth factor receptor 2/keratinocyte growth factor receptor. *Clin. Cancer Res.* **2007**, *13*, 3051–3057.
- (20) Kunii, K.; Davis, L.; Gorenstein, J.; Hatch, H.; Yashiro, M.; Di Bacco, A.; Elbi, C.; Lutterbach, B. FGFR2-amplified gastric cancer cell lines require FGFR2 and Erbb3 Signaling for Growth and Survival. *Cancer Res.* **2008**, *68*, 2340–2348.
- (21) Pollock, P. M.; Gartside, M. G.; Dejeza, L. C.; Powell, M. A.; Mallon, M. A.; Davies, H.; Mohammadi, M.; Futreal, P. A.; Stratton, M. R.; Trent, J. M.; Goodfellow, P. J. Frequent activating FGFR2 mutations in endometrial carcinomas parallel germline mutations associated with craniosynostosis and skeletal dysplasia syndromes. *Oncogene* **2007**, *26*, 7158–7162.
- (22) Weiss, J. M.; Sos, M. L.; Seidel, D.; Peifer, M.; Zander, T.; Heuckmann, J. M.; Ullrich, R. T.; Menon, R.; Maier, S.; Soltermann, A.; Moch, H.; Wagener, P.; Fischer, F.; Heynck, S.; Koker, M.; Schöttle, J.; Leenders, F.; Gabler, F.; Dabow, I.; Querings, S.; Heukamp, L. C.; Balke-Want, H.; Ansén, S.; Rauh, D.; Baessmann, I.; Altmüller, J.; Wainer, Z.; Conron, M.; Wright, G.; Russell, O.; Solomon, B.; Brambilla, E.; Brambilla, C.; Lorimier, P.; Sollberg, S.; Brustugun, O. T.; Engel-Riedel, W.; Ludwig, C.; Petersen, I.; Sängler, J.; Clement, J.; Groen, H.; Timens, W.; Sietsma, H.; Thunnissen, E.; Smit, E.; Heideman, D.; Cappuzzo, F.; Ligorio, C.; Damiani, S.; Hallek, M.; Beroukham, R.; Pao, W.; Klebl, B.; Baumann, M.; Buettner, R.; Ernestus, K.; Stoelben, E.; Wolf, J.; Nürnberg, P.; Perner, S.; Thomas, R. K. Frequent and Focal FGFR1 Amplification Associates with Therapeutically Tractable FGFR1 Dependency in Squamous Cell Lung Cancer. *Sci. Transl. Med.* **2010**, *2*, 62–93.
- (23) Reis-Filho, J. S.; Simpson, P. T.; Turner, N. C.; Lambros, M. B.; Jones, C.; Mackay, A.; Grigoriadis, A.; Sarrio, D.; Savage, K.; Dexter, T.; Irvani, M.; Fenwick, K.; Weber, B.; Hardisson, D.; Schmitt, F. C.; Palacios, J.; Lakhani, S. R.; Ashworth, A. FGFR1 emerges as a potential therapeutic target for lobular breast carcinomas. *Clin. Cancer Res.* **2006**, *12*, 6652–6662.
- (24) Penault-Llorca, F.; Bertucci, F.; Adelaide, J.; Parc, P.; Coulier, F.; Jacquemier, J.; Birnbaum, D.; deLapeyriere, O. Expression of FGF and FGF receptor genes in human breast cancer. *Int. J. Cancer* **1995**, *61*, 170–176.
- (25) Jacquemier, J.; Adelaide, J.; Parc, P.; Penault-Llorca, F.; Planche, J.; deLapeyriere, O.; Birnbaum, D. Expression of the FGFR1 gene in human breast-carcinoma cells. *Int. J. Cancer* **1994**, *59*, 373–378.
- (26) Jaakkola, S.; Salmikangas, P.; Nylund, S.; Partanen, J.; Armstrong, E.; Pyrhonen, S.; Lehtovirta, P.; Nevanlinna, H. Amplification of fgfr4 gene in human breast and gynecological cancers. *Int. J. Cancer* **1993**, *54*, 378–382.
- (27) Theillet, C.; Adelaide, J.; Louason, G.; Bonnet-Dorion, F.; Jacquemier, J.; Adnane, J.; Longy, M.; Katsaros, D.; Sismondi, P.; Gaudray, P.; et al. FGFR1 and PLAT genes and DNA amplification at 8p12 in breast and ovarian cancers. *Genes, Chromosomes Cancer* **1993**, *7*, 219–226.
- (28) Adnane, J.; Gaudray, P.; Dionne, C. A.; Crumley, G.; Jaye, M.; Schlessinger, J.; Jeanteur, P.; Birnbaum, D.; Theillet, C. BEK and FLG, two receptors to members of the FGF family, are amplified in subsets of human breast cancers. *Oncogene* **1991**, *6*, 659–663.
- (29) Elsheikh, S. E.; Green, A. R.; Lambros, M. B. K.; Turner, N. C.; Grainge, M. J.; Powe, D.; Ellis, I. O.; Reis-Filho, J. S. FGFR1 amplification in breast carcinomas: a chromogenic in situ hybridisation analysis. *Breast Cancer Res.* **2007**, *9*, R23.
- (30) Valladares, A.; Garcia Hernandez, N.; Salamanca Gomez, F.; Curiel-Quezada, E.; Madrigal-Bujaidar, E.; Vergara, M. D.; Sierra Martinez, M.; Arenas Aranda, D. J. Genetic expression profiles and chromosomal alterations in sporadic breast cancer in Mexican women. *Cancer Genet. Cytogenet.* **2006**, *170*, 147–151.
- (31) Fioravanti, L.; Cappelletti, V.; Coradini, D.; Miodini, P.; Borsani, G.; Daidone, M. G.; Di Fronzo, G. int-2 oncogene amplification and prognosis in node-negative breast carcinoma. *Int. J. Cancer* **1997**, *74*, 620–624.
- (32) Hui, R.; Campbell, D. H.; Lee, C. S. L.; McCaul, K.; Horsfall, D. J.; Musgrove, E. A.; Daly, R. J.; Seshadri, R.; Sutherland, R. L. EMS1 amplification can occur independently of CCND1 or INT-2 amplification at 11q13 and may identify different phenotypes in primary breast cancer. *Oncogene* **1997**, *15*, 1617–1623.
- (33) Berns, E. M. J. J.; Foekens, J. A.; van Staveren, I. L.; van Putten, W. L. J.; de Koning, H. Y. W. C. M.; Portengen, H.; Klijn, J. G. M. Oncogene amplification and prognosis in breast cancer: relationship with systemic treatment. *Gene* **1995**, *159*, 11–18.
- (34) Mayr, D.; Kanitz, V.; Anderegg, B.; Luthardt, B.; Engel, J.; Lohrs, U.; Amann, G.; Diebold, J. Analysis of gene amplification and prognostic markers in ovarian cancer using comparative genomic hybridization for microarrays and immunohistochemical analysis for tissue microarrays. *Am. J. Clin. Pathol.* **2006**, *126*, 101–109.
- (35) Seki, A.; Yoshinouchi, M.; Seki, N.; Kodama, J.; Miyagi, Y.; Kudo, T. Detection of c-erbB-2 and FGF-3 (INT-2) gene amplification in epithelial ovarian cancer. *Int. J. Oncol.* **2000**, *17*, 103–106.
- (36) Rubin, J. S.; Qiu, L.; Etkind, P. Amplification of the Int-2 gene in head and neck squamous cell carcinoma. *J. Laryngol. Otol.* **1995**, *109*, 72–76.
- (37) Hu, L.; Sham, J. S. T.; Xie, D.; Wen, J.-M.; Wang, W.-S.; Wang, Y.; Guan, X.-Y. Up-regulation of fibroblast growth factor 3 is associated with tumor metastasis and recurrence in human hepatocellular carcinoma. *Cancer Lett.* **2007**, *252*, 36–42.
- (38) Tsou, A. P.; Wu, K. M.; Tsen, T. Y.; Chi, C. W.; Chiu, J. H.; Lui, W. Y.; Hu, C. P.; Chang, C.; Chou, C. K.; Tsai, S. F. Parallel hybridization analysis of multiple protein kinase genes: identification of gene expression patterns characteristic of human hepatocellular carcinoma. *Genomics* **1998**, *50*, 331–340.
- (39) Gerald, J.; Heckel, A.; Colbatzky, F.; Handschuh, S.; Kley, J.; Lehmann-Lintz, T.; Lotz, R.; Tontsch-Grunt, U.; Walter, R.; Hilberg, F. Design, Synthesis, and Evaluation of Indolinones as Triple Angiokinase Inhibitors and the Discovery of a Highly Specific 6-Methoxycarbonyl-Substituted Indolinone (BIBF 1120). *J. Med. Chem.* **2009**, *52*, 4466–4480.
- (40) Renhowe, P. A.; Pecchi, S.; Shafer, C. M.; Machajewski, T. D.; Jazan, E. M.; Taylor, C.; Antonios-McCrea, W.; McBride, C. M.; Frazier, K.; Wiesmann, M.; Lapointe, G. R.; Feucht, P. H.; Warne, R. L.; Heise, C. C.; Menezes, D.; Aardalen, K.; Ye, H.; He, M.; Le, V.; Vora, J.

Jansen, J. M.; Wernette-Hammond, M. E.; Harris, A. L. Design, Structure–Activity Relationships and in Vivo Characterization of 4-Amino-3-benzimidazol-2-ylhydroquinolin-2-ones: A Novel Class of Receptor Tyrosine Kinase Inhibitors. *J. Med. Chem.* **2009**, *52*, 278–292.

(41) Bhide, R. S.; Cai, Z.-W.; Zhang, Y.-Z.; Qian, L.; Wei, D.; Barbosa, S.; Lombardo, L. J.; Borzilleri, R. M.; Zheng, X.; Wu, L. L.; Barrish, J. C.; Kim, S.-H.; Leavitt, K.; Mathur, A.; Leith, L.; Chao, S.; Wautlet, B.; Mortillo, S.; Jayaseelan, R., Sr.; Kukral, D.; Hunt, J.; Kamath, A.; Fura, A.; Vyas, V.; Marathe, P.; D'Arienzo, C.; Derbin, G.; Fargnoli, J. Discovery and preclinical studies of (R)-1-(4-(4-fluoro-2-methyl-1H-indol-5-yloxy)-5-methylpyrrolo[2,1-f][1,2,4]triazin-6-yloxy)propanol (BMS-540215), an in vivo active potent VEGFR-2 inhibitor. *J. Med. Chem.* **2006**, *49*, 2143–2146.

(42) Hennequin, L. F. A.; Ple, P.; Stokes, E. S. E.; Mckerrecher, D. Quinazoline derivatives as angiogenesis inhibitors. Patent WO2000047212, 2000.

(43) Wedge, S. R.; K. J.; Hennequin, L. F.; Valentine, P. J.; Barry, S. T.; Brave, S. R.; Smith, N. R.; James, N. H.; Dukes, M.; Curwen, J. O.; Chester, R.; Jackson, J. A.; Boffey, S. J.; Kilburn, L. L.; Barnett, S.; Richmond, G. H. P.; Wadsworth, P. F.; Walker, M.; Bigley, A. L.; Taylor, S. T.; Cooper, L.; Beck, S.; Jurgensmeier, J. M.; Ogilvie, D. J. AZD2171: a highly potent, orally bioavailable, vascular endothelial growth factor receptor-2 tyrosine kinase inhibitor for the treatment of cancer. *Cancer Res.* **2005**, *65*, 4389–4400.

(44) Moussy, A.; Kinet, J.-P. Use of dual C-KIT/FGFR3 inhibitors for treating multiple myeloma. Patent WO2007026251, 2007.

(45) Sun, L.; Tran, N.; Liang, C.; Tang, F.; Rice, A.; Schreck, R.; Waltz, K.; Shawver, L. K.; McMahon, G.; Tang, Cho. Design, Synthesis, and Evaluations of Substituted 3-[(3- or 4-Carboxyethylpyrrol-2-yl)-methylidene]indolin-2-ones as Inhibitors of VEGF, FGF, and PDGF Receptor Tyrosine Kinases. *J. Med. Chem.* **1999**, *42*, 5120–5130.

(46) Huang, W.-S.; Metcalf, C. A.; Sundaramoorthi, R.; Wang, Y.; Zou, D.; Thomas, R. M.; Zhu, X.; Cai, L.; Wen, D.; Liu, S.; Romero, J.; Qi, J.; Chen, I.; Banda, G.; Lentini, S. P.; Das, S.; Xu, Q.; Keats, J.; Wang, F.; Wardwell, S.; Ning, Y.; Snodgrass, J. T.; Broudy, M. I.; Russian, K.; Zhou, T.; Commodore, L.; Narasimhan, N. I.; Mohemmad, Q. K.; Iulicci, J.; Rivera, V. M.; Dalgarno, D. C.; Sawyer, T. K.; Clackson, T.; Shakespeare, W. C. Discovery of 3-[2-(Imidazo[1,2-b]pyridazin-3-yl)-ethynyl]-4-methyl-N-[4-((4-methylpiperazin-1-yl)methyl)-3-(trifluoromethyl)phenyl]benzamide (AP24534), a Potent, Orally Active Pan-Inhibitor of Breakpoint Cluster Region–Abelson (BCR-ABL) Kinase Including the T315I Gatekeeper Mutant. *J. Med. Chem.* **2010**, *53*, 4701–4719.

(47) Funahashi, Y.; Tsuruoka, A.; Matsukura, M.; Haneda, T.; Fukuda, Y.; Kamata, J.; Takahashi, K.; Matsushima, T.; Miyazaki, K.; Nomoto, K.; Watanabe, T.; Obaishi, H.; Yamaguchi, A.; Suzuki, S.; Nakamura, K.; Mimura, F.; Yamamoto, Y.; Matsui, J.; Matsui, K.; Yoshida, T.; Suzuki, Y.; Arimoto, I. Nitrogenous aromatic ring compounds. Patent WO2002032872, 2002.

(48) Matsui, J.; Yamamoto, Y.; Funahashi, Y.; Tsuruoka, A.; Watanabe, T.; Wakabayashi, T.; Uenaka, T.; Asada, M. E7080, a novel inhibitor that targets multiple kinases, has potent antitumor activities against stem cell factor producing human small cell lung cancer H146, based on angiogenesis inhibition. *Int. J. Cancer* **2007**, *122*, 664–671.

(49) During the preparation of this manuscript, AstraZeneca disclosed the FGFR inhibitor AZD4547. Gavine, P. R.; Mooney, L.; Kilgour, E.; Thomas, A. P.; Al-Kadhimi, K.; Beck, S.; Coleman, T.; Baker, D.; Mellor, M. J.; Brooks, A. N.; Klinowska, T. Characterization of AZD4547: An orally bioavailable, potent and selective inhibitor of FGFR tyrosine kinases 1, 2 and 3. American Association for Cancer Research (AACR) 102nd Annual Meeting, Orlando, FL, April 2–6, 2011, Abstract 3568.

(50) Furet, P.; Caravatti, G.; Guagnano, V.; Lang, M.; Meyer, T.; Schoepfer, J. Entry into a new class of protein kinase inhibitors by pseudo ring design. *Bioorg. Med. Chem. Lett.* **2008**, *18*, 897–900.

(51) The kinase domains of FGFR2, FGFR3 and FGFR4 have a sequence identity to that of FGFR1 of 87%, 84%, and 75%, respectively. In the ATP binding site, all the residues are conserved within the different isoforms with the exception of two of them located in the hinge region and corresponding to FGFR3 residues Y557 and A559.

In FGFR1 and FGFR2, Y557 is conserved while it is mutated into a cysteine in FGFR4. A559 is conserved in FGFR4 but is a serine in FGFR1 and FGFR2. The latter residue points towards the exterior of the ATP pocket and cannot make contact with inhibitors. In contrast, Y557 and its cysteine equivalent in FGFR4 can make van der Waals contacts with inhibitors.

(52) Thompson, A. M.; Delaney, A. M.; Hamby, J. M.; Schroeder, M. C.; Spoon, T. A.; Crean, S. M.; Showalter, H. D. H.; Denny, W. A. Synthesis and Structure–Activity Relationships of Soluble 7-Substituted 3-(3,5-Dimethoxyphenyl)-1,6-naphthyridin-2-amines and Related Ureas as Dual Inhibitors of the Fibroblast Growth Factor Receptor-1 and Vascular Endothelial Growth Factor Receptor-2 Tyrosine Kinases. *J. Med. Chem.* **2005**, *48*, 4628–4653.

(53) Mohammadi, M.; Froum, S.; Hamby, J. M.; Schroeder, M. C.; Panek, R. L.; Lu, G. H.; Eliseenkova, A. V.; Green, D.; Schlessinger, J.; Hubbard, S. R. Crystal structure of an angiogenesis inhibitor bound to the FGF receptor tyrosine kinase domain. *EMBO J.* **1998**, *17*, 5896–5904.

(54) Ong, S. H.; Guy, G. R.; Hadari, Y. R.; Laks, S.; Gotoh, N.; Schlessinger, J.; Lax, I. FRS2 proteins recruit intracellular signaling pathways by binding to diverse targets on fibroblast growth factor and nerve growth factor receptors. *Mol. Cell. Biol.* **2000**, *20*, 979–989.

(55) Mohamadi, F.; Richards, N. G. J.; Guida, W. C.; Liskamp, R.; Lipton, M.; Caufield, C.; Chang, G.; Hendrickson, T.; Still, W. C. MacroModel—an integrated software system for modeling organic and bioorganic molecules using molecular mechanics. *J. Comput. Chem.* **1990**, *11*, 440–467.

(56) Bairoch, A.; Boeckmann, B. The SWISS-PROT protein sequence data bank: current status. *Nucleic Acids Res.* **1994**, *22*, 3578–3580.

(57) Notredame, C.; Higgins, D.; G.; Heringa, J. T.-Coffee: A novel method for fast and accurate multiple sequence alignment. *J. Mol. Biol.* **2000**, *302*, 205–217.

(58) Vriend, G. WHAT IF: A molecular modeling and drug design program. *J. Mol. Graphics* **1990**, *8*, 52–56.

(59) Bailey, S. The CCP4 suite: programs for protein crystallography. *Acta Crystallogr., Sect. D: Biol. Crystallogr.* **1994**, *D50*, 760–763.

(60) Bricogne, G.; Blanc, E.; Brandl, M.; Flensburg, C.; Keller, P.; Paciorek, P.; Roversi, P.; Sharff, A.; Smart, O.; Vonrhein, C.; Womans, T. *Buster 2.9*; Global Phasing Ltd.: Cambridge, UK2010.